

Article

Post-Impact Faulting of the Holfontein Granophyre Dike of the Vredefort Impact Structure, South Africa, Inferred from Remote Sensing, Geophysics, and Geochemistry

Martin D. Clark ^{1,*}, Elizaveta Kovaleva ², Matthew S. Huber ¹, Francois Fourie ³ and Chris Harris ⁴

¹ Department of Geology, University of the Free State, 205 Nelson Mandela Drive, Bloemfontein 9300, South Africa; HuberMS@ufs.ac.za

² Department of Earth Science, University of the Western Cape, Robert Sobukwe Road, Belville 7535, South Africa; myzikant88@gmail.com

³ Institute for Groundwater Studies, University of the Free State, 205 Nelson Mandela Drive, Bloemfontein 9300, South Africa; FourieFD@ufs.ac.za

⁴ Department of Geological Sciences, University of Cape Town, Rondebosch 7700, South Africa; chris.harris@uct.ac.za

* Correspondence: clarkmd@ufs.ac.za; Tel.: +27-51-401-3892



Citation: Clark, M.D.; Kovaleva, E.; Huber, M.S.; Fourie, F.; Harris, C. Post-Impact Faulting of the Holfontein Granophyre Dike of the Vredefort Impact Structure, South Africa, Inferred from Remote Sensing, Geophysics, and Geochemistry. *Geosciences* **2021**, *11*, 96. <https://doi.org/10.3390/geosciences11020096>

Academic Editors:
Jesus Martinez-Frias and Steven J. Jaret

Received: 28 December 2020
Accepted: 7 February 2021
Published: 19 February 2021

Publisher's Note: MDPI stays neutral with regard to jurisdictional claims in published maps and institutional affiliations.



Copyright: © 2021 by the authors. Licensee MDPI, Basel, Switzerland. This article is an open access article distributed under the terms and conditions of the Creative Commons Attribution (CC BY) license (<https://creativecommons.org/licenses/by/4.0/>).

Abstract: Better characterization features borne from long-term crustal modification processes is essential for understanding the dynamics of large basin-forming impact structures on Earth. Within the deeply eroded 2.02 Ga Vredefort Impact Structure in South Africa, impact melt dikes are exposed at the surface. In this study, we utilized a combination of field, remote sensing, electrical resistivity, magnetic, petrographical, and geochemical techniques to characterize one such impact melt dike, namely, the Holfontein Granophyre Dike (HGD), along with the host granites. The HGD is split into two seemingly disconnected segments. Geophysical modeling of both segments suggests that the melt rock does not penetrate below the modern surface deeper than 5 m, which was confirmed by a later transecting construction trench. Even though the textures and clast content are different in two segments, the major element, trace element, and O isotope compositions of each segment are indistinguishable. Structural measurements of the tectonic foliations in the granites, as well as the spatial expression of the dike, suggest that the dike was segmented by an ENE–WSW trending sinistral strike-slip fault zone. Such an offset must have occurred after the dike solidified. However, the Vredefort structure has not been affected by any major tectonic events after the impact occurred. Therefore, the inferred segmentation of the HGD is consistent with long-term crustal processes occurring in the post-impact environment. These crustal processes may have involved progressive uplift of the crater floor, which is consistent with post-impact long-term crustal adjustment that has been inferred for craters on the Moon.

Keywords: deep crust; post-impact deformation; meteorite impact; Kaapvaal Craton

1. Introduction

The Vredefort Impact Structure in South Africa is one of the oldest and largest known impact structures on Earth and forms an impact basin (Figure 1A) [1]. Such impact basins form voluminous melt sheets on the surface that feed dikes, which descend into underlying country rocks at the late stages of the impact cratering process [2]. At Vredefort, these intrusions are known as Vredefort Granophyre Dikes (e.g., [3]). The dikes are the only remnant of the melt sheet, which was removed by post-impact erosion, and, therefore, represent the unique opportunity to study the impact melt at Vredefort and processes related to their emplacement and post-emplacement deformation [4,5].

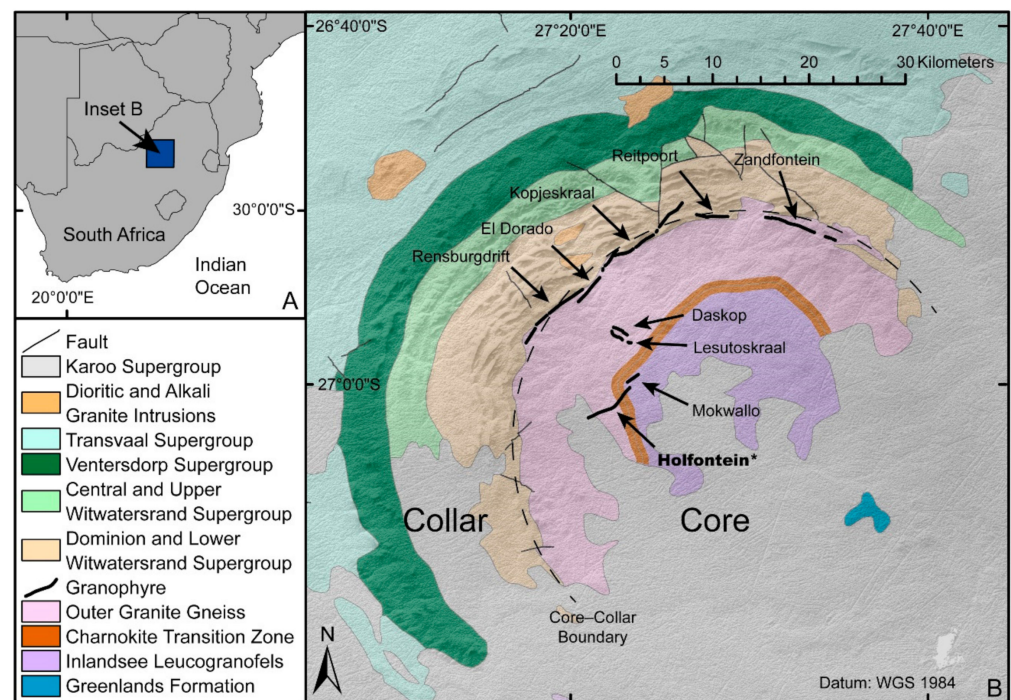


Figure 1. Generalized geological map of the Vredefort Impact Structure. (A) Location of the Vredefort Impact Structure in South Africa. (B) Surface geology and prominent structures associated with the Vredefort Impact Structure. The stratigraphy and structure from the South African Council for Geosciences, granophyre dikes locations according to [3]. The studied dike is indicated by *. The topography is generated from the Advanced Spaceborne Thermal Emission and Reflection Radiometer Global Digital Elevation Map (ASTER GDEM). ASTER GDEM is a product of the Ministry of Economy, Trade, and Industry (METI) of Japan and the United States National Aeronautics and Space Administration (NASA).

The Granophyre Dikes are analogous to another set of impact melt dikes known as the Offset Dikes of the Sudbury impact structure in Canada [6]. Unlike the Vredefort Granophyre Dikes, the Offset Dikes have been reworked by several orogenic events [7,8]. The dikes at Vredefort appear to be free from any significant first-order deformation features that are associated with tectonic events. The structure as a whole has retained its circular expression, and due to its location within the Kaapvaal Craton, has not undergone any significant tectonic reworking since the impact occurred at 2020 ± 2 Ma (Figure 1B) [9–11].

The Vredefort Granophyre Dikes are found at nine locations in the Vredefort Impact Structure (Figure 1B): in the 40–50 km diameter central portion of the impact structure, referred to as the core of the central uplift, and along the boundary of the core with the younger, topographically accentuated surrounding strata, termed the collar of the central uplift (Figure 1). At the core, the dikes are radial, sub-radial, or concentric to the central portion of the impact, while at the collar, they are concentric.

One of the core dikes, the Holfontein Granophyre Dike, is expressed as two semi-continuous segments (north and south), which slightly differ in width and orientation. The Holfontein Granophyre Dike is found at the southern margin of the town of Vredefort, where township development projects are steadily reducing its exposure. Although the Holfontein Granophyre Dike has been extensively studied with the focus on its petrography and geochemistry [3,12,13], no structural investigations have been done on-site. Moreover, the granites in the immediate surrounding area of the Holfontein Granophyre Dike were excluded from previous analyses. Therefore, this study aimed to provide a structural, petrographic, geochemical, and geophysical assessment of the granophyre segments and these granites in order to better understand the emplacement and post-emplacement history of the Holfontein Granophyre Dike.

In particular, we analyzed whether the current spatial configuration of two segments of the dike is a primary feature, or whether it occurred after the emplacement of the dike. Two groups of processes, which post-date the impact, could have a bearing on the configuration observed: those of tectonic origin [10,11,14] and processes associated with post-impact crustal adjustment in large impact craters [15], of which, the latter could have resulted in the dike's emplacement [16,17]. A combination of analytical techniques was applied, including unmanned aerial vehicle (UAV)-borne aerial photography, structural observation, geophysical investigation, petrography, and bulk and isotopic geochemistry. By completing a comprehensive analytical study of the granophyre dike and its host rocks, we aimed to obtain a better understanding of the granophyre's exposure in terms of multiple segments and their orientation and thickness. As no subsurface studies have been done on the Holfontein Granophyre Dike, this study aimed to document and interpret its underground expression.

2. General Geology

2.1. Geology of the Vredefort Impact Structure

The 2019 ± 2 Ma Vredefort Impact Structure [9], located in the center of the Witwatersrand Basin, had an estimated initial diameter of 250–300 km [5,18]. At present, the Vredefort Impact Structure is composed of a core of 3.3–3.08 Ga Archean crystalline basement rocks and a surrounding collar of 3.07 Ga to 2.10 Ga metavolcanic and metasedimentary rocks [19]. The Archean crystalline basement rocks include a central zone of granulite facies granofels called the Inlandsee Leucogranofels (ILG) [20], and a surrounding zone of amphibolite facies granite gneiss known as the Outer Granite Gneiss (OGG) [19,21]. Between the two units, the zone of charnockitic gneiss known as the Charnockite Transition Zone (CTZ) is observed [19]. The surrounding collar area is characterized by overturned strata to various degrees belonging to the Dominion Group, and the Transvaal, Ventersdorp, and Witwatersrand Supergroups [22]. The contact between the collar and the core is only exposed on the northeast, northwest, and west (Figure 1B). In the south and east, volcano-sedimentary rocks of the Karoo Supergroup mask the presence of underlying rocks, except for limited exposures of Greenland's Greenstone Complex [23].

Granophyre dikes are found in the core and at the core–collar boundary and are only exposed at the surface in the northern and western portions of the structure [3,12,16]. Dikes in the core are up to 4–5 km long and less than 20 m wide, while dikes in the core–collar boundary are up to 9 km long and up to 65 m wide (Figure 1B) [12]. The dikes generally crop out as continuous lines of disaggregated outcrops, or, less frequently, as discontinuous pavements with sharp contacts. The dikes occur both as clast-rich and clast-poor varieties, where the former have an inhomogeneous distribution of clasts both across and along the strike [2,3,13]. Clast-rich zones are characterized by up to 70 vol.% clasts with an average clast content of 10–20 vol.% [13,24]. Granophyre dikes can be texturally characterized as spherulitic or granular varieties [3,24]. Further references regarding studies on the Vredefort Granophyre Dikes are given by [25].

2.2. Holfontein Granophyre Dike: Field Observations

The Holfontein Granophyre Dike (HGD) is expressed at the surface as two linear arrangements of boulders, namely, Holfontein north (HGD-N) and Holfontein south (HGD-S). The height of the outcrop above the ground does not exceed 0.5 m for the HGD-N and ≈ 1.5 m for the HGD-S. The northern part of HGD-N has in recent years been covered by a pigsty and a township. Overall, the HGD-N and HGD-S dikes are roughly parallel, but in plan view, have an increasing curvature away from each other toward the NE (Figure 2). Gaps between the groups of boulders are present along the strike of the dikes and are either an erosional feature or a result of anthropogenic development. The preserved part of the HGD-N is a ≈ 380 m long segment, oriented NNE–SSW, while the HGD-S is a ≈ 200 m long segment oriented NEE–SSW.

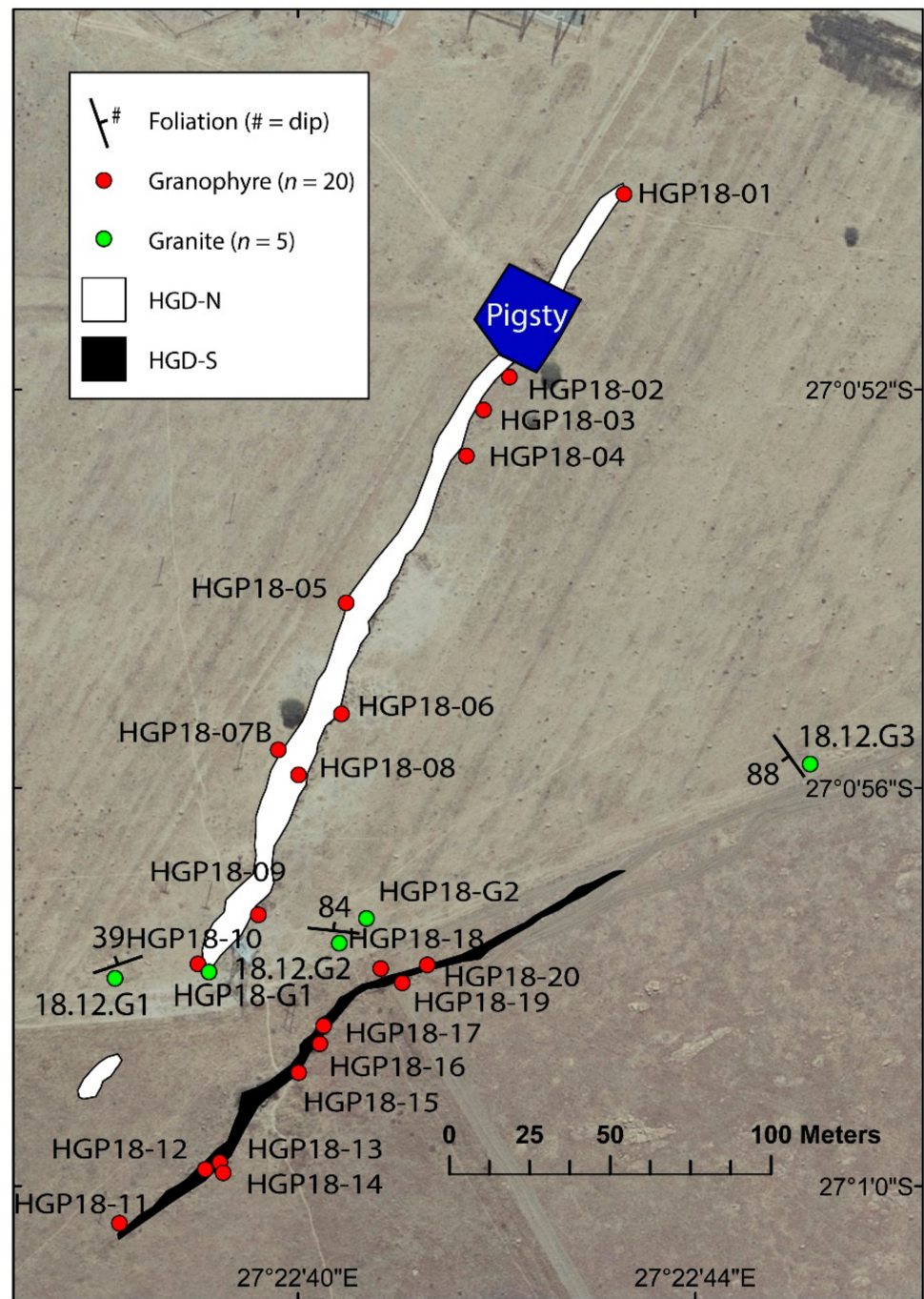


Figure 2. An aerial photograph with sampling locations and foliation directions of the Holfontein Granophyre Dyke (HGD) and the surrounding granite. Continuous patches of granophyre are indicated by white (HGD north (HGD-N)) and black (HGD south (HGD-S)) polygons.

The two dike segments have textural distinctions in the field [13]. HGD-N contains on average < 10 vol.% of clasts, its matrix has spherulitic textures, and it does not contain pegmatitic veins. By contrast, HGD-S has inhomogeneously distributed clasts, with a 1 m wide section at the north margin of the dike containing > 10 vol.% clasts, but the remainder of the dike contains < 10 vol.% clasts. HGD-S does not have a spherulitic texture in the matrix and contains pegmatitic veins [13]. The pegmatitic veins are oriented subparallel to the margins of the dike segment, vary in thickness between 4 and 20 cm, and have the same proportion of lithic clasts as the hosting portions of granophyre [13].

3. Methods and Samples

3.1. Field and Aerial Observations

Field and aerial observations were completed over two field excursions on 20 November 2018 and from 8 to 12 August 2019. Structural field observations were made using a Freiberg geological structure compass (Clar Notation: Dip Direction/Dip) and a small unmanned aerial vehicle (sUAV) quadcopter, a DJI Mavic 2 Pro with DJI Go 4 software. The DJI Mavic 2 Pro has a 1" complementary metal oxide semiconductor (CMOS) imaging sensor that can take still images at a resolution of 5472×3648 pixels, and videos at a resolution of "4 K" (3840×2160 pixels). Two methods of still image capture were employed, namely, direct still image capture and extraction of still images (frames) from videos. The extraction of frames was accomplished using Agisoft Photoscan Pro v.1.4.3 software. Images were captured at an altitude of 15–30 m to collect high-resolution imagery of the study area and avoid any flight obstacles. Imagery and structural measurements were analyzed using Esri ArcMap v.10.4.

3.2. Sampling

The sampling of the granophyre was conducted at semi-regular intervals of ≈ 10 m along the strike of the two dike segments. Samples were collected by a Husqvarna channel saw with a diamond cutting wheel. Ten samples were collected from each segment of the dike, 20 samples in total. For the sampling of HGD-S, permission was granted by the owner of the property where the dike is found. Adjacent granites were sampled using a channel saw with a diamond cutting wheel, as the exposure was limited to low-lying rounded outcrops. Five samples were collected from the host granites in three sets: G1 (HGP18-G1, 18-12-G1), G2 (HGP18-G2, 18-12-G2), and G3 (18-12-G3). The sampling locations are indicated in Figure 2.

3.3. Ground Magnetic Survey

Ground magnetic data were recorded across HGD-N on a grid consisting of seven lines with west–east orientations (L01 to L07), one line perpendicular to the outcrop (L08), and a single tie-line (T01) with a south–north orientation (Figure 3). The purpose of line L08 was to accurately define the shape of the magnetic anomaly associated with the dike. An attempt was made to also record magnetic data on a line (L09) perpendicular to the outcrop of HGD-S; however, an overhead powerline that runs approximately parallel to this part of the dike caused excessive electromagnetic noise, preventing the line from extending across the dike.

The presence of infrastructure limited the survey area to a trapezoidal region bounded by overhead powerlines in the east, west, and south, and an electrical substation in the north. A fenced pigsty in the center of the survey area was another source of noise that had to be avoided during the survey. The line separation on the grid was approximately 25 m, except where the pigsty forced one line (L03) to deviate from its west–east course (Figure 3). Magnetic data were recorded with the GEM GSM19-W system using a sampling interval of 0.2 s, resulting in an average station spacing of approximately 0.3 m.

The magnetic data were processed by first removing all erratic data near the western and eastern limits of the survey lines where the influence of the overhead powerlines affected the survey. The magnetic data were subsequently leveled with respect to the tie-line. All data processing and mapping was done using the Oasis montaj™ v.8 software of Seequent®.

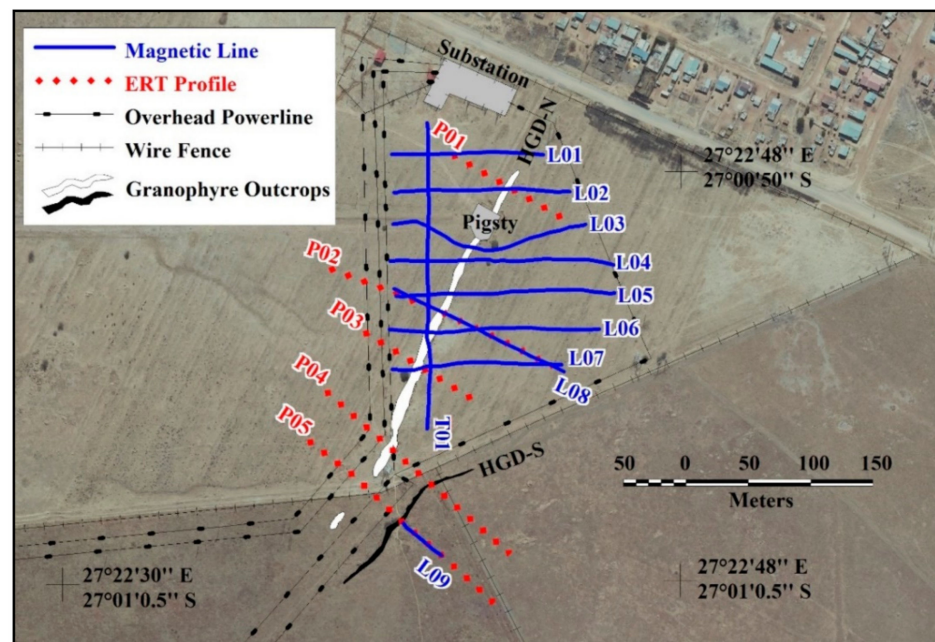


Figure 3. Positions and orientations of the magnetic lines and electrical resistivity tomography (ERT) profiles across the Holfontein Granophyre Dike (black lines) plotted on top of an aerial photo.

3.4. Electrical Resistivity Tomography (ERT) Survey

An ERT survey was done on five profiles that were approximately perpendicular to the outcrops of HGD-N and HGD-S (P01 to P05 lines in Figure 3). Apparent resistivity data were recorded using the Lund Imaging System (Terrameter SAS1000, Electrode Selector ES10-64C and multicore cables) supplied by Guideline Geo AB. A unit electrode spacing of 2.5 m was employed on profiles P02, P04, and P05, while a unit electrode spacing of 1.25 m was used on profiles P01 and P03 to allow for a higher spatial resolution. Profiles P02, P04, and P05 thus had lengths of 200 m, whereas profiles P01 and P03 were 100 m long. The Schlumberger electrode geometry was used on all profiles.

Data processing was limited to the removal of outliers from the apparent resistivity datasets. The datasets were subsequently inverted to obtain models of the subsurface resistivity distribution in the vicinity of the dike(s). Inversion was done with the software package Res2DInv v3.58 developed by Geotomo Software Sdn Bhd using an algorithm employing the L1 norm to allow for models with sharp boundaries between the different geological units in the subsurface.

3.5. Optical Microscopy and Scanning Electron Microscopy (SEM)

Optical microscopy and SEM imaging of the Holfontein granophyre and its surrounding granites were undertaken at the Department of Geology at the University of the Free State using the polished petrographic thin sections. The equipment used was an Olympus BX51 optical microscope with an attached Olympus U-TVO.63XC camera; the carbon-coated thin sections were studied using a Jeol JSM-6610 SEM equipped with an energy-dispersive Thermo Scientific Ultradry energy-dispersive X-ray (EDX) spectrometer. The EDX detector was used to qualitatively identify mineral phases. The analytical conditions for collecting the backscattered electron (BSE) images were a 15 kV accelerating voltage, 8 nA probe current, and 10 mm working distance.

3.6. Major and Trace Element Laboratory Analyses

Samples from the Holfontein Granophyre Dike and surrounding granites were analyzed for major and trace elements in the wavelength-dispersive X-ray fluorescence spectrometer (WD-XRF) laboratory at the Department of Geology, University of the Free

State. Samples were crushed into a powder, which was used to prepare fusion discs (used for elements of major quantities) and pressed pellets (used to measure Na and trace elements). The chemical analyses of major elements were conducted with the sequential PANalytical Axios WD-XRF machine using “IGS majors” and “Sodium only” applications accordingly. The XRF data for trace elements were obtained from the pressed pellets on the same spectrometer using an end-window Rh X-ray tube. Calibration was performed using a set of 20–40 well-characterized natural rock standards that were issued by agencies such as the United States Geology Survey (USGS), Geochemical Reference samples Database (GSJ), and Mintek. Raw data were processed with the X-ray analyses software SuperQ 4.0R with the toolbox for trace elements Pro-Trace (PANalytical B.V.). The statistical method applied to the obtained analyses was a two-tailed *t*-test, $p < 0.0001$.

3.7. Isotope Geochemistry

Oxygen isotopes were determined on whole-rock powder via the conventional method using externally-heated Ni bombs [26], employing ClF_3 as a reagent at 550 °C for 4 h and converting the liberated O_2 to CO_2 . All measurements were made offline using a Finnegan DeltaXP mass spectrometer in dual inlet mode. All data are reported in δ -notation, where $\delta^{18}\text{O} = (R_{\text{sample}}/R_{\text{standard}} - 1) \times 1000$; R is the measured $^{18}\text{O}/^{16}\text{O}$ ratio and standard mean ocean water (SMOW) was the standard. Duplicate splits of the in-house standard matrix quartz (MQ) were run with each batch of eight samples to monitor analytical precision and convert the raw data to the SMOW scale using the $\delta^{18}\text{O}$ value of 10.1‰ for MQ (calibrated against a value of $\delta^{18}\text{O}$ value of 9.64‰ from the National Bureau of Standards (NBS)-28. The long-term variability of MQ suggested a 2σ error of 0.16‰.

4. Results

4.1. Field and Aerial Observations

The positions of the two segments of the dike are shown in Figure 2 (aerial still image and videos available at <https://doi.org/10.38140/ufs.13698817.v2> (accessed on 3 February 2021)). The southern terminus of the NNE–SSW-trending HGD-N segment was not exposed as it approached the HGD-S segment. Parallel and west of the HGD-S segment, there was a small 2–3 m patch of granophyre boulders, which appeared to be in line with the HGD-N segment. The northern extent of the HGD-S segment was curved toward the east while its southern terminus trended southwest. The two dike segments varied in lateral width, where HGD-N was 7–11 m, and HGD-S was 1–6 m in width. HGD-N was notably more disaggregated with 1–4 m gaps between the outcrop patches, while HGD-S was more aggregated and compact, with a much higher density of outcrops that defined its width (Figure 4A–C).

HGD-S contained pegmatitic veins [13] and was clast-rich with clasts that were notably larger (1.5–5.0 cm in length) than clasts in HGD-N and elongated (Figure 4D). HGD-N had spherulitic textures and was clast-poor with clasts being rounded and small (<1.5 cm) (Figure 4E).

Country granites sporadically formed outcrops in the field in adjacent areas next to and between the two dike segments. The granite outcrops were generally smooth and did not elevate above the ground higher than 0.5 m. Within the area shown in Figure 4A, variation in the granite textures and composition was observed. Pink granites (e.g., sample HGP18-G2) were found primarily northeast and northwest of HGD-S, and grey massive granites (e.g., samples 18.12.G1 and HGP18-G1) were located west of HGD-S, while grey foliated granite (e.g., sample 18.12.G3) was found to the northeast (Figure 2). Some granite outcrops to the northeast of the two dike segments displayed pseudotachylite veins. Pink foliated charnockite was found in the outcrop directly between the dike segments (sample 18.12.G2).

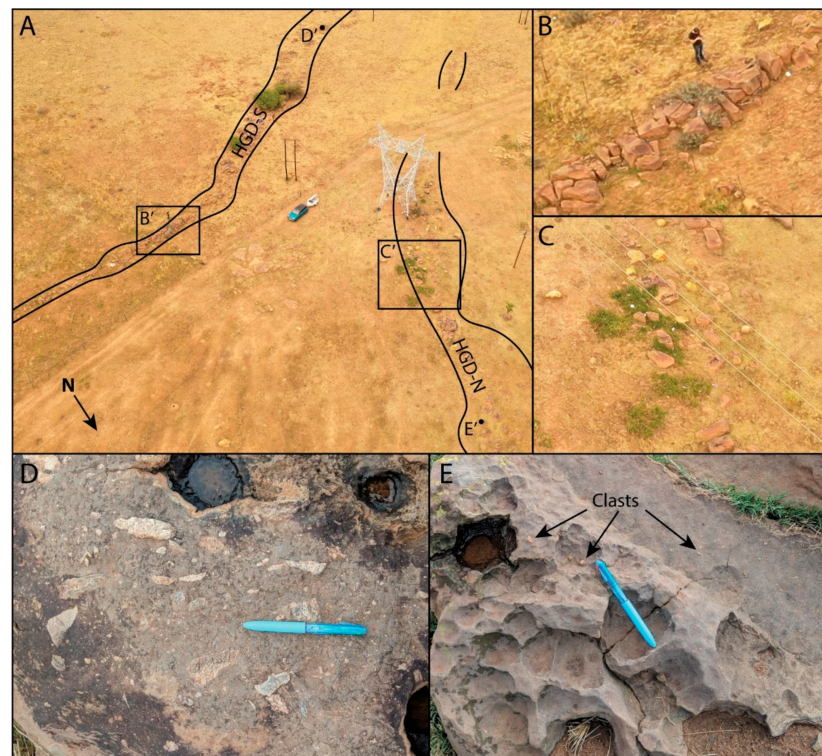


Figure 4. Southwest-facing unmanned aerial vehicle (UAV) image showing disaggregate and aggregate characteristics of the HGD-N and HGD-S dike segments, respectively. Bounding black lines of the dike segments roughly indicate the dike margins. (A) Note the car and trailer for scale. (B) Referencing inset B' on HGD-S showing a characteristic compact dike segment. The width of the dike was $\approx 2\text{--}3$ m. Note the person for scale. (C) Referencing inset C' on HGD-N showing a characteristic disaggregated dike segment. The width of the dike at this section was ≈ 6 m and this inset was diagnostic of the segment. (D) Referencing point D' in A, which is a photo of large angular clasts in the matrix of HGD-S. (E) Referencing point E' in A, a photo of small clasts in the matrix of HGD-N. Note the prominent erosional pits. In images D and E, note the pen (14 cm) for scale.

Structural markers in the granites were scarce in the area due to limited exposures. Two northward dipping foliations (341/39, 006/84) were measured on granites directly adjacent to and between the two dike segments respectively, and one southwestward dipping foliation (234/88) was measured east of HGD-S (Figure 2). Lineations were not apparent.

4.2. Ground Magnetic Survey

A strong magnetic response was recorded across HGD-N. The magnetic anomaly associated with the dike displayed a large negative trough above the dike with a smaller positive peak immediately east of the dike. Examples of the magnetic data recorded along lines L02, L03, and L04 are presented as profile plots with the position of the dike indicated (HGD-N; Figure 5). Although the dike anomaly had an amplitude of several hundreds of nanotesla (nT), other magnetic anomalies with amplitudes exceeding 500 nT were observed over the basement rocks to the west (L02) and east (L04) of the dike. The magnetic data recorded perpendicularly across the dike on L08 displayed similar properties to the other profiles (Figure 5). The dike yielded a negative magnetic anomaly, which was dominated by a more prominent negative anomaly located to the southeast of the dike.

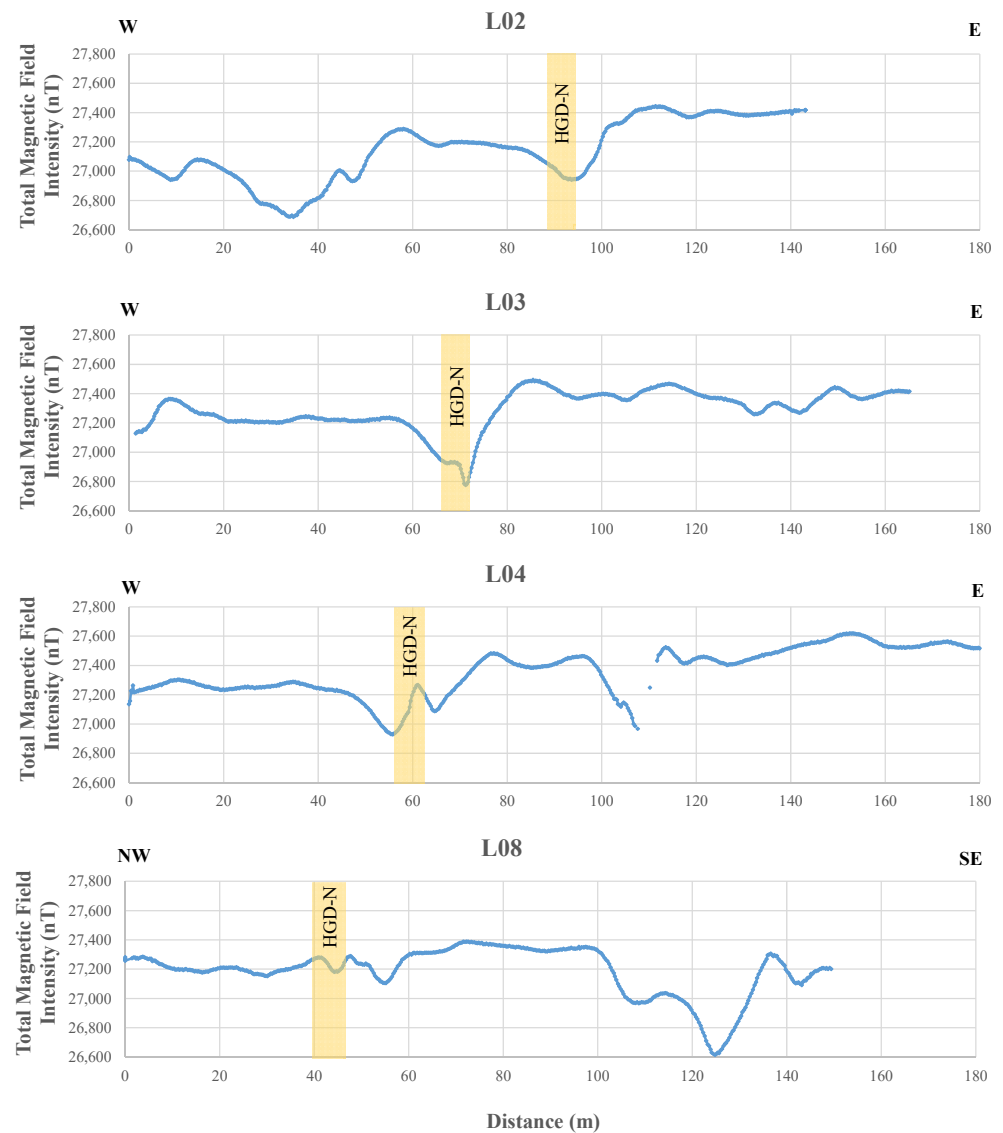


Figure 5. Profile plots of the total magnetic field recorded along the lines L02, L03, L04, and L08.

A contour map of the total magnetic field recorded across HGD-N is shown in Figure 6. The coherent magnetic signature of the dike, as well as the variable and magnetic response over the Archean basement rocks, are seen in the map (Figure 6). A large negative anomaly occurred west of the dike, while a prominent positive anomaly was observed to the east.

4.3. Electrical Resistivity Tomography Survey

The inverse resistivity models obtained for the five ERT profiles are shown in Figure 7. To allow for a direct comparison, only the central 100 m of profiles P02, P04, and P05 are shown such that all the modeled sections have the same lateral and depth extents. The resistivity models are displayed using linear color scales (instead of logarithmic scales) to emphasize the greater resistivity contrasts in the models. Even with this emphasis on the larger contrasts, the inverse resistivity models revealed the complexity of the subsurface. Although some of the profiles were separated by <50 m, they displayed very different resistivity distributions. However, all models revealed that the granophyre outcrops were associated with zones of high resistivity.

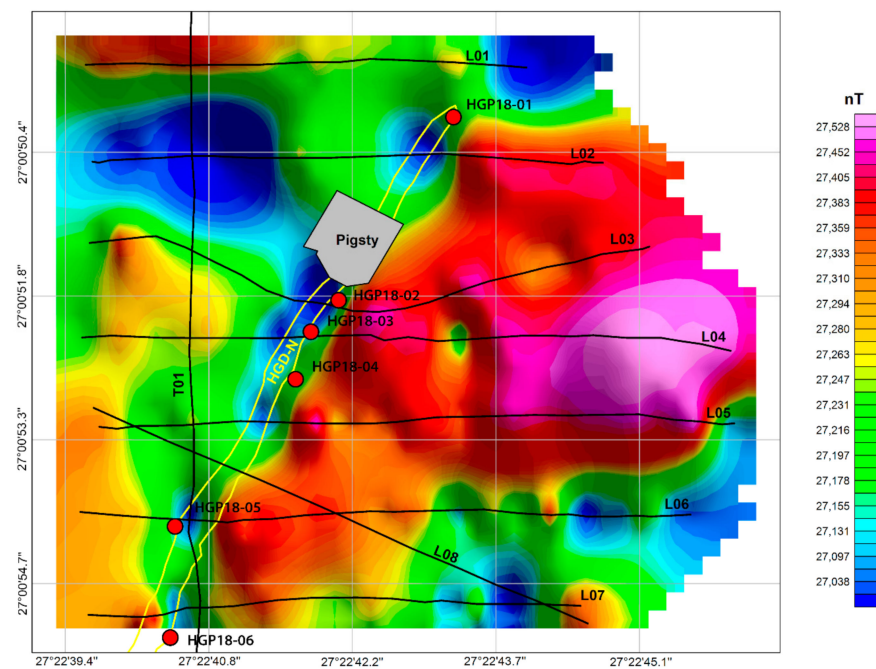


Figure 6. Contour map of the total magnetic field intensity recorded across the northern outcrop of the Holfontein Granophyre Dike (HGD-N). Data collection lines are indicated in black. Geological samples are indicated with red points.

The profiles that intersected only HGD-N (P01 to P03) showed that the dike was associated with resistivities $>700 \Omega\text{m}$. The zones of high resistivities were seen to have a disaggregated appearance and extended only a few meters ($<3 \text{ m}$) into the subsurface. The penetration depths on P01 and P03 appeared to be particularly low ($<1.5 \text{ m}$). Along profile P04, the resistivity of the dike was seen to be lower ($\approx 300 \Omega\text{m}$), possibly due to a higher degree of weathering. In this profile, the dike also seemed to be in contact with a deeper body of high resistivity. Profile P04 extended across HGD-S. In this profile, HGD-S had a much higher resistivity (off the scale in P04 but $>4000 \Omega\text{m}$ in P05) and a more compact character than HGD-N, which was an observation confirmed by the resistivity model of profile P05. Along the P05 profile, HGD-S was seen to be associated with a very localized zone of extremely high resistivities ($>10,000 \Omega\text{m}$) that extended to a depth of approximately 4 m (Figure 7, P05). The results of the ERT survey, therefore, suggest that HGD-S had a limited penetration depth.

4.4. Optical Microscopy and SEM

4.4.1. Granophyre

HGD-N was spherulitic to granular, with large spherules up to 3 cm in diameter. HGD-S had an intersertal to porphyritic igneous texture, was medium-to-fine-grained, except for the pegmatitic veins, which were coarse-grained (for more details, see [13]). The elongated laths of the orthopyroxene were up to 0.5–1.0 mm in length and were randomly oriented. The interstitial space was filled with plagioclase and quartz. Plagioclase occurred as spherical or elongated aggregates that were spreading outward. The clasts were mainly composed of mosaic quartz, were abundant, and varied in size from a few mm to several cm (Figure 8). Spinel, K-feldspar, and biotite were accessory minerals. More details on the granophyre petrography and various textural types, such as that in HGD-N, are given in [3,24].

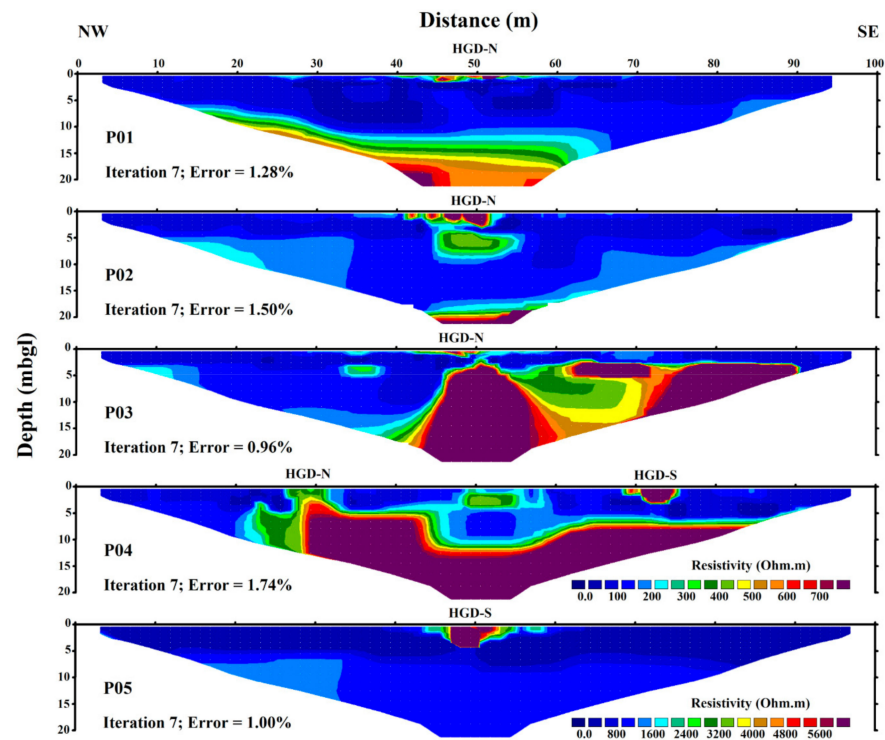


Figure 7. Modeled resistivity sections across the HGD-N and HGD-S outcrops. The legend for profiles P01–P04 is located in profile P04. Due to the much higher resistivities recorded along profile P05, a different color scale is used for the resistivity model of this profile. m bgl: meters below ground level.

4.4.2. Host Granites

The granites were coarse-grained, locally foliated, and composed of quartz, plagioclase, K-feldspar, biotite, and \pm orthopyroxene as major phases. In thin sections, they showed undulatory extinction of quartz and feldspars, and less frequently, they showed mosaic extinction. In all samples, the grain boundaries between the phases were irregular and cusped-lobate (Figure 9). All samples contained biotite and opaque phases with lobate boundaries. The plagioclase in all samples was fractured and had curvilinear cleavage (e.g., Figure 9D). In the SEM images, these features were decorated with a BSE lighter phase, possibly sericite and/or K-feldspar (Figure 9A). Plagioclase was frequently twinned, significantly altered, especially along the twin boundaries, and possibly sericitized. In all samples, quartz showed planar deformation features (PDFs) and was fractured and re-crystallized to fine-grained aggregates along the non-planar and planar fractures (Figure 9E).

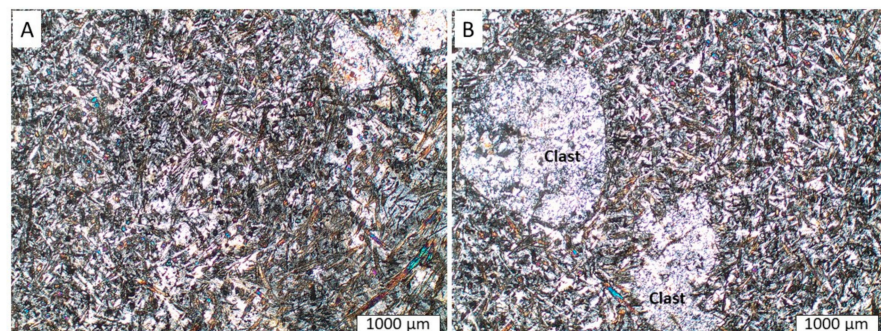


Figure 8. (A,B) Photomicrographs in crossed-polarized light (XPL) of the thin section representing typical HGD-S (fine-grained intersertal to porphyritic igneous texture as in [13]). The light domains are lithic clasts, predominantly composed of mosaic quartz.

Sample 18.12.G1: Grey massive granite that was leucocratic and comparatively coarse-crystalline (Figure 9A). Main phases: quartz, plagioclase, K-feldspar, and biotite. The grain size was 1 mm on average, but varied from 0.5 to 3 mm, and could rarely be up to 5 mm. The grains were elongated and had irregular, lobate boundaries. The sample contained rare biotite grains, up to 3 mm in size, made of opaque minerals (mostly iron oxide minerals, but also rutile with small crystals of ilmenite within, and ilmenite), and large accessory zircons. About 50% of all biotite grains were decomposed to a fine-grained mixture of iron oxides, quartz, chlorite, and a Ca-bearing phase, possibly clinopyroxene. Locally, biotite needles were intergrown with quartz.

Sample HGP18-G1: Grey massive granite, where in the hand-sample, it had a “sugary” appearance. This sample was finer-grained compared to the others, possibly mylonitized. The grains were from 100–200 μm to 1 mm in size. Abundant curvilinear features in the plagioclase were observed. Small tabular and intersertal grains of biotite that were 100–300 μm in size were abundant. Biotite was commonly (about 50%) replaced by chlorite and quartz and had a poikilitic texture (Figure 9B). Intersertal opaque iron oxide phases up to 1 mm in size with lobate boundaries were observed, but they were less common than in the other samples. Quartz had a finer grain size and evidence of recrystallization in the matrix. Some small (100–200 μm) rounded quartz grains were enclosed in the plagioclase or occur along the phase boundaries.

Sample 18.12.G2: Pink foliated granite with lineation that was rich in mafic minerals composed of coarse grains (1–3 mm in size). The rock-forming minerals were plagioclase, quartz, biotite, and orthopyroxene; K-feldspar was an accessory phase. Large aggregates of biotite were locally replaced by chlorite and recrystallized quartz, which was associated with opaque phases. Abundant inclusions of apatite, monazite, and zircon in the biotite and orthopyroxene were observed. Chlorite frequently truncated/replaced the biotite. The opaque phases were rutile, ilmenite, and iron oxide minerals. Large (up to 3 mm) elongate grains of orthopyroxene were observed, with rounded grain boundaries that were intensely fractured and altered along the fractures, with abundant inclusions of apatite (Figure 9C).

Sample HGP18-G2: Coarse-grained pink granite that was weakly foliated. The rock-forming phases were plagioclase, quartz, biotite, and K-feldspar. The latter revealed the lamellae of plagioclase. Plagioclase, in turn, had lamellae of quartz (myrmekites). The grains were from 1 to 4 mm in size. The sample had abundant biotite associated with opaque phases (mainly iron oxide minerals), abundant apatite, and zircon. Large grains of monazite (up to 1 mm) were present. Biotite was locally decomposed to chlorite and K-feldspar (about 20%). A few quartz grains showed planar fractures with fine-grained texture along their length. The plagioclase revealed curvilinear features (Figure 9D).

Sample 18.12.G3: Gray foliated coarse-to-medium-grained granite. The grains varied in size from 0.5 to 2 mm. Plagioclase had K-feldspar and quartz lamellae (myrmekites). Biotite was common, it formed foliation, and was associated with opaque phases (ilmenite, rutile, and iron oxide minerals; rarely zinc sulfide) and very abundant apatite. The biotite aggregates (about 40%) locally decomposed into calcite, fine crystals of iron oxide, chlorite, quartz, and K-feldspar. The quartz had sets of planar features and was recrystallized along the fractures (possibly former PDFs; Figure 9E). Large (up to 1 mm) grains of monazite revealed closely spaced planar features and were present in association with biotite, apatite, and opaque minerals (Figure 9F).

4.5. Major and Trace Element Results

The granophyre samples showed little variation in composition and were similar to previously published bulk analyses of the Vredefort granophyre [12,13]. For both HGD-N and HGD-S, there was no statistical difference in the abundances of major elements. The granophyre had a major elemental composition of 66.7 ± 0.6 wt.% SiO_2 , 12.6 ± 0.2 wt.% Al_2O_3 , 7.1 ± 0.2 wt.% Fe_2O_3 , 3.6 ± 0.1 wt.% CaO , 2.7 ± 0.1 wt.% Na_2O , and 2.3 ± 0.1 wt.% K_2O . The trace element compositions of the HGD-N and HGD-S were also similar (Table 1), with both dikes having a Cr/Ni ratio of 2.0. Using the Total Alkali-Silica (TAS) classifica-

tion scheme [27], the Holfontein granophyre was identified to be dacitic in composition (Figure 10A). The high-field-strength elements (HFSE) for both HGD-N and HGD-S had identical patterns (Figure 10B).

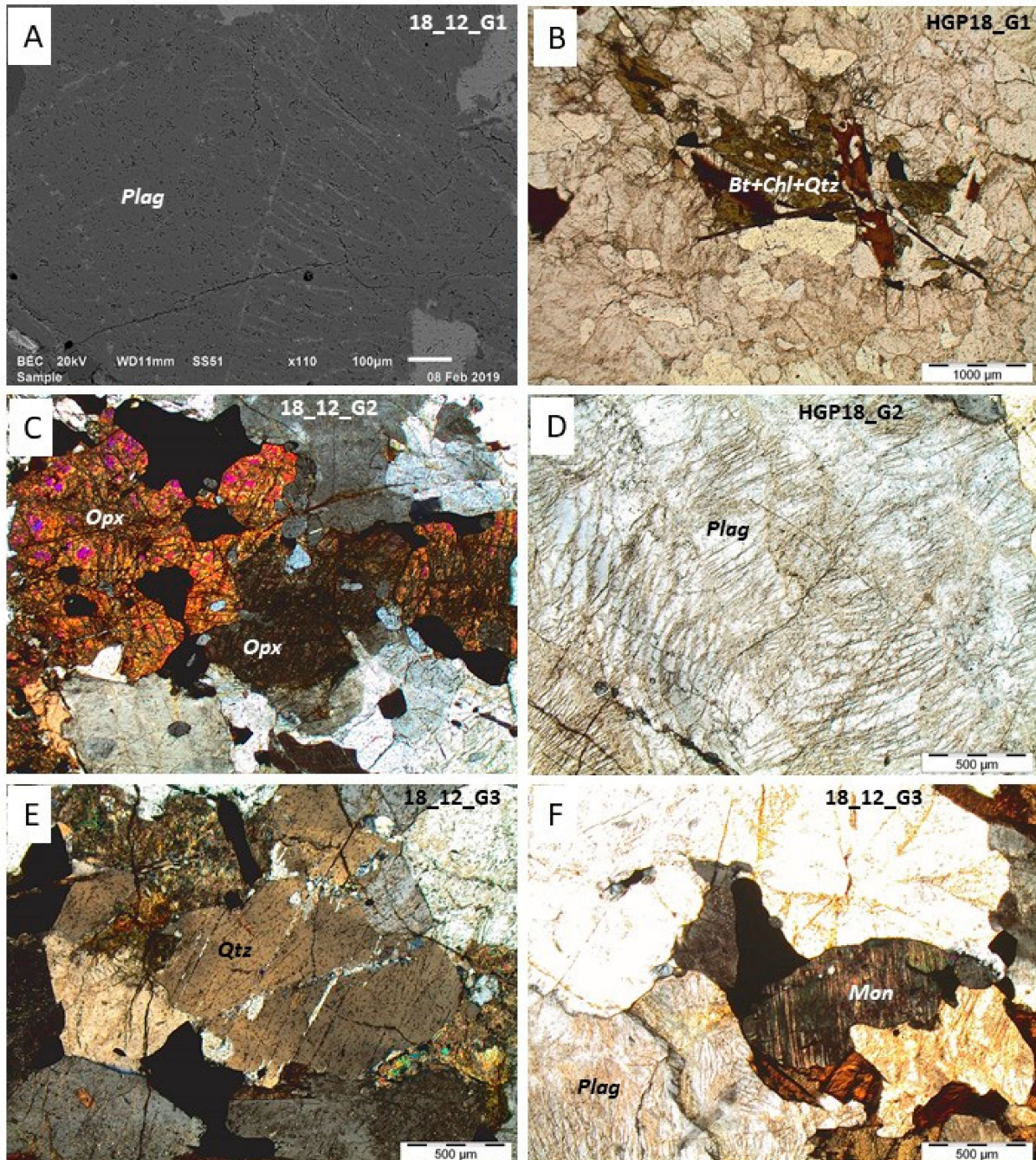


Figure 9. (A) Backscattered electron (BSE) image of plagioclase in sample 18_12_G1. (B) Sample HGP18_G1 in plane-polarized light (PPL). (C) Orthopyroxene crystals (high interference color) with apatite (grey crystals enclosed in Opx) in sample 18_12_G2 in crossed-polarized light (XPL). Scale as in (B). (D) Plagioclase with “feather” features in sample HGP18_G2 (PPL). (E) Recrystallization along the planar deformation features (PDFs) in quartz in sample 18_12_G3 (XPL). (F) Chocked monazite found in sample 18_12_G3 (XPL). Planar microstructures extended in the N–S direction. Bt: biotite, Chl: chlorite, Mon: monazite, Opx: orthopyroxene, Plag: plagioclase, Qtz: quartz.

Table 1. Major (wt.%) and trace (ppm) element data for granophyre and granitoid samples.

	Holfontein Granophyre Dike—North Segment												Holfontein Granophyre Dike—South Segment								Granitoids							
	HGP18-01	HGP18-02	HGP18-03	HGP18-04	HGP18-05	HGP18-06	HGP18-07B	HGP18-08	HGP18-09	HGP18-10	HGP18-11	HGP18-12	HGP18-13	HGP18-14	HGP18-15	HGP18-16	HGP18-17	HGP18-18	HGP18-19	HGP18-20	HGP18-G1	18-12-G1A	18-12-G1B	HGP18-G2	18-12-G2A	18-12-G2B	18-12-G3	
Lat	-27.0139	-27.01441	-27.01452	-27.01463	-27.01504	-27.01535	-27.01545	-27.01552	-27.01591	-27.01606	-27.01677	-27.01662	-27.0166	-27.01663	-27.01635	-27.01622	-27.01627	-27.01606	-27.0161	-27.01605	-27.016054	-27.016078	-27.016078	-27.015918	-27.051998	-27.051998	-27.051998	-27.051496
Long	27.37869	27.37837	27.37831	27.37825	27.37787	27.37790	27.37771	27.37778	27.37769	27.37749	27.37728	27.37752	27.37756	27.37757	27.37778	27.37785	27.37784	27.37801	27.37807	27.37814	27.37754	27.37725	27.37725	27.37798	27.37791	27.37791	27.37791	27.37920
SiO ₂	66.6	65.6	65.8	66.8	65.7	66.7	65.7	67.0	67.7	66.8	67.4	66.6	66.1	66.9	66.6	67.1	66.8	67.3	66.9	67.5	69.2	70.4	72.6	69.8	64.5	64.4	66.1	
TiO ₂	0.51	0.56	0.52	0.47	0.54	0.52	0.52	0.48	0.52	0.49	0.46	0.50	0.46	0.49	0.5	0.46	0.49	0.47	0.47	0.48	0.29	0.49	0.50	0.50	0.93	1.18	0.75	
Al ₂ O ₃	12.6	12.6	12.6	12.7	12.4	12.7	12.0	12.8	13.0	12.6	12.6	12.6	12.6	12.7	12.6	12.5	12.6	12.6	12.7	12.6	16.9	15.9	14.4	15.9	16.5	16.8	16.2	
Fe ₂ O ₃ T	7.22	7.20	7.19	7.02	7.28	7.22	6.83	6.91	7.24	7.03	6.89	7.27	7.33	7.15	7.14	6.95	7.12	6.95	7.08	6.99	2.01	3.20	2.77	2.87	5.49	5.88	4.21	
MnO	0.14	0.14	0.14	0.13	0.13	0.14	0.13	0.13	0.13	0.14	0.13	0.14	0.14	0.14	0.14	0.14	0.14	0.13	0.14	0.13	0.02	0.04	0.04	0.03	0.05	0.07	0.04	
MgO	3.62	3.20	3.50	3.38	3.82	3.32	3.14	3.16	3.24	3.29	3.21	3.51	4.19	3.64	3.77	3.57	3.33	3.43	3.56	3.52	0.77	0.62	0.68	0.62	1.44	1.54	1.16	
CaO	3.62	3.73	3.67	3.54	3.59	3.67	3.57	3.47	3.68	3.62	3.47	3.63	3.77	3.66	3.67	3.5	3.62	3.45	3.58	3.53	3.01	2.93	2.44	2.26	3.20	3.57	3.20	
Na ₂ O	2.79	2.77	2.8	2.68	2.67	2.87	2.5	2.65	2.61	2.76	2.76	2.89	2.85	2.87	2.99	2.67	2.75	2.83	2.61	2.53	5.07	4.30	4.30	3.79	3.96	4.39	3.80	
K ₂ O	2.29	2.32	2.27	2.34	2.31	2.32	2.21	2.38	2.36	2.35	2.34	2.27	2.12	2.36	2.31	2.31	2.34	2.33	2.34	2.38	2.22	1.58	1.89	3.62	3.05	2.28	2.40	
P ₂ O ₅	0.10	0.12	0.11	0.09	0.11	0.11	0.11	0.10	0.11	0.10	0.09	0.10	0.09	0.10	0.10	0.09	0.10	0.09	0.10	0.10	0.09	0.08	0.05	0.19	0.41	0.44	0.33	
LOI	0.13	0.21	0.01	0.00	0.01	0.02	0.10	0.01	0.22	0.00	0.01	0.01	0.00	0.00	0.00	0.07	0.01	0.00	0.00	0.00	0.83	0.70	0.67	0.78	0.79	0.65	0.86	
Total	99.7	98.4	98.6	99.1	98.6	99.6	93.8	99.1	100.7	99.3	99.4	99.5	99.6	99.9	99.8	99.3	99.3	98.9	99.3	99.7	100.5	100.2	100.3	100.3	100.4	101.3	99.0	
Sc	16	15	20	20	18	18	12	17	12	16	17	20	16	17	17	15	15	17	20	19	4	0	0	0	5	6	4	
V	87	91	88	82	92	87	87	84	87	85	84	88	85	88	85	83	84	85	85	84	5	35	26	27	56	53	49	
Cr	250	199	229	254	244	232	200	250	222	237	246	244	247	235	240	244	259	254	255	7	11	6	12	20	20	16		
Co	27	25	27	27	27	27	25	27	28	26	29	28	27	27	28	26	25	27	26	9	13	13	12	24	24	20		
Ba	471	471	467	457	452	462	448	488	461	464	464	464	441	453	473	458	452	467	458	468	867	538	709	1495	1410	1118	986	
Ni	121	101	113	119	117	117	103	121	112	115	118	121	123	117	115	123	117	124	121	119	7	5	9	10	9	14	12	
Cu	53	52	54	53	53	56	54	57	51	54	53	55	57	54	51	53	57	54	52	5	15	14	10	21	38	6		
Zn	65	58	58	45	66	59	57	61	66	55	56	59	53	54	61	69	56	66	60	59	31	64	63	39	71	84	60	
Rb	66	66	65	69	66	67	67	67	67	68	69	65	60	69	67	67	68	68	67	67	33	23	30	80	56	39	61	
Sr	254	263	260	251	256	256	255	267	252	252	249	251	259	250	252	247	251	254	255	257	760	670	628	761	798	839	706	
Y	17	18	17	16	17	17	17	16	17	17	16	16	16	16	16	16	16	16	16	16	3	3	3	8	12	13	10	
Zr	144	151	144	142	148	144	148	147	145	144	141	140	130	143	143	142	143	145	144	144	135	347	276	341	334	393	298	
Nb	7	8	7	7	7	7	7	7	7	7	7	7	7	7	7	7	7	7	7	7	6	8	9	10	16	21	10	
Mo	2	2	2	2	2	2	2	2	2	2	2	2	2	2	3	3	2	4	2	2	1	b.d.l.	b.d.l.	b.d.l.	b.d.l.	b.d.l.	b.d.l.	
Pb	14	10	11	12	12	13	12	12	11	12	13	10	12	13	12	11	11	13	12	14	12	37	24	34	19	18	19	
Th	6	7	6	7	6	7	6	7	6	6	7	6	6	6	7	7	6	6	8	6	b.d.l.	68	32	31	15	13		
U	2	3	b.d.l.	b.d.l.	b.d.l.	b.d.l.	3	b.d.l.	b.d.l.	4	b.d.l.	2	2	3	2	b.d.l.	b.d.l.	3	b.d.l.	b.d.l.	b.d.l.	b.d.l.	1	b.d.l.	3	b.d.l.	b.d.l.	
d ¹⁸ O	7.4	6.9	7.1	7.0	8.6	7.6	7.8	7.8	7.7	8.7	7.5	7.3	7.5	7.6	7.8	7.3	7.6	7.4	7.1	7.4								

b.d.l.: below detection limit; Lat: latitude, Long: longitude. Latitude and longitude in decimal degrees; Fe₂O₃T: total Fe as Fe₂O₃.

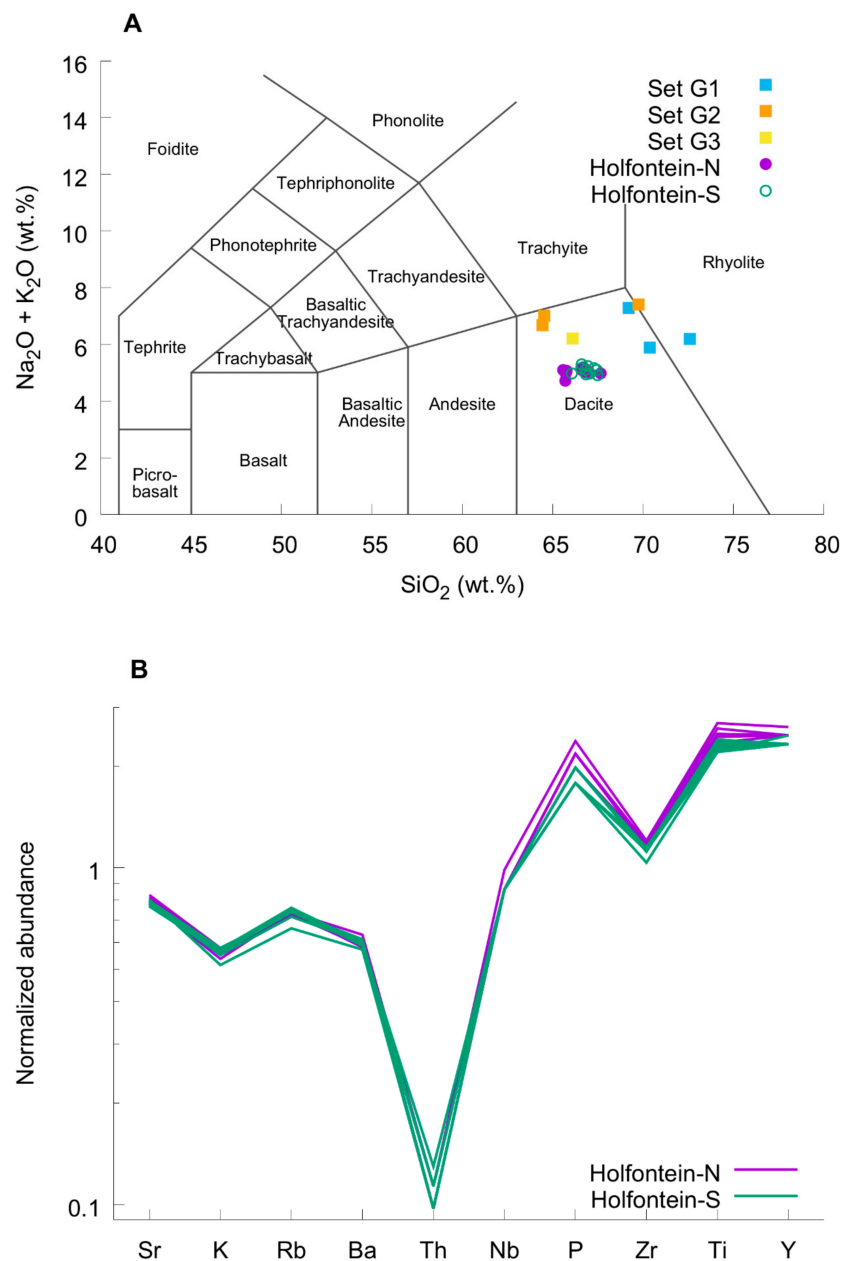


Figure 10. (A) Classification of the host granites and granophyre on the total alkali–silica diagram from [27]. (B) High-field-strength elements of HGD-N and HGD-S. The granophyre compositions were normalized to the average granite compositions measured in this study.

The SiO₂ content of the host granites varied, as samples 18.12.G1 and HGP18-G1 had highly silicic compositions, with SiO₂ ranging from 69.2 to 72.6 wt.%, sample HGP18-G2 had similar SiO₂ content, with 69.7 wt.%, but sample 18.12.G2 (charnockite) had a SiO₂ content of 64.5 wt.%, which was similar to sample 18.12.G3 with 66.1 wt.% SiO₂ (Table 1, Figure 10A). All samples were granodiorites (Figure 11), although they did not overlap on the ternary Ab–An–Or graph (Figure 11). The granodiorites straddled the boundary between ferroan and magnesian classifications (Figure 12a) [28], and varied from alkalic (charnockitic) to calc-alkaline (Figure 12b). Regarding the trace elements, the G1 sample set defined a distinct population from G2 and G3 (Figure 13), with a significantly lower abundance of Y, Rb, Nb, and Sr than the other samples analyzed.

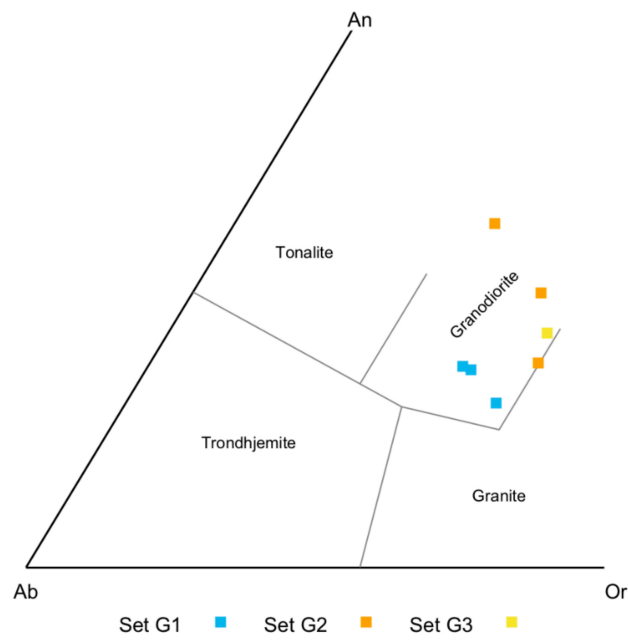


Figure 11. Quadrant of [29] granite classification with normalized feldspar endmembers. An: Anorthite, Ab: Albite, Or: Orthoclase.

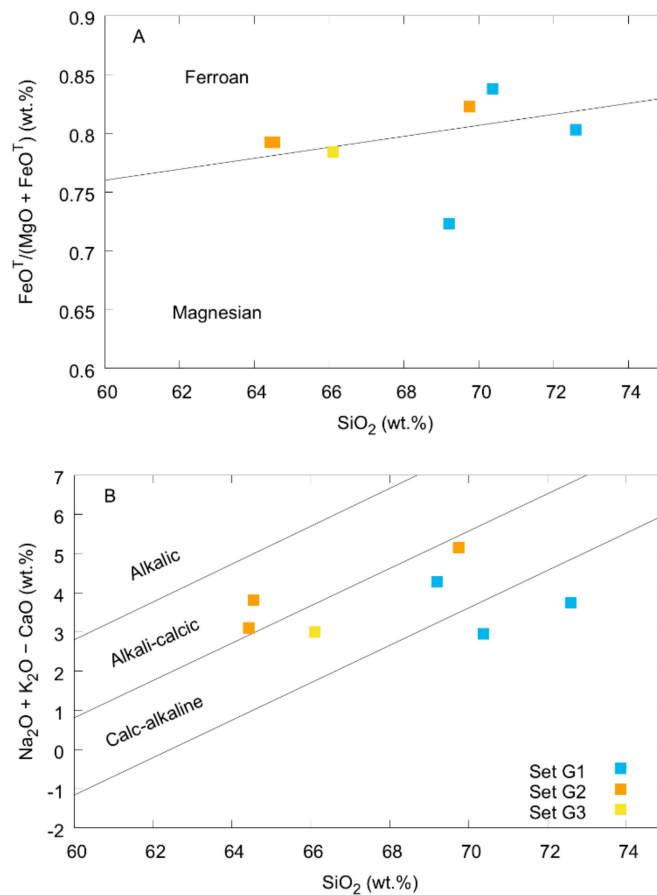


Figure 12. Classification of the granitoid samples in this study using the scheme of [28]. The granitoids varied between magnesian and ferroan (A) and ranged from calc-alkaline to alkali-calcic, but were not alkalic (B).

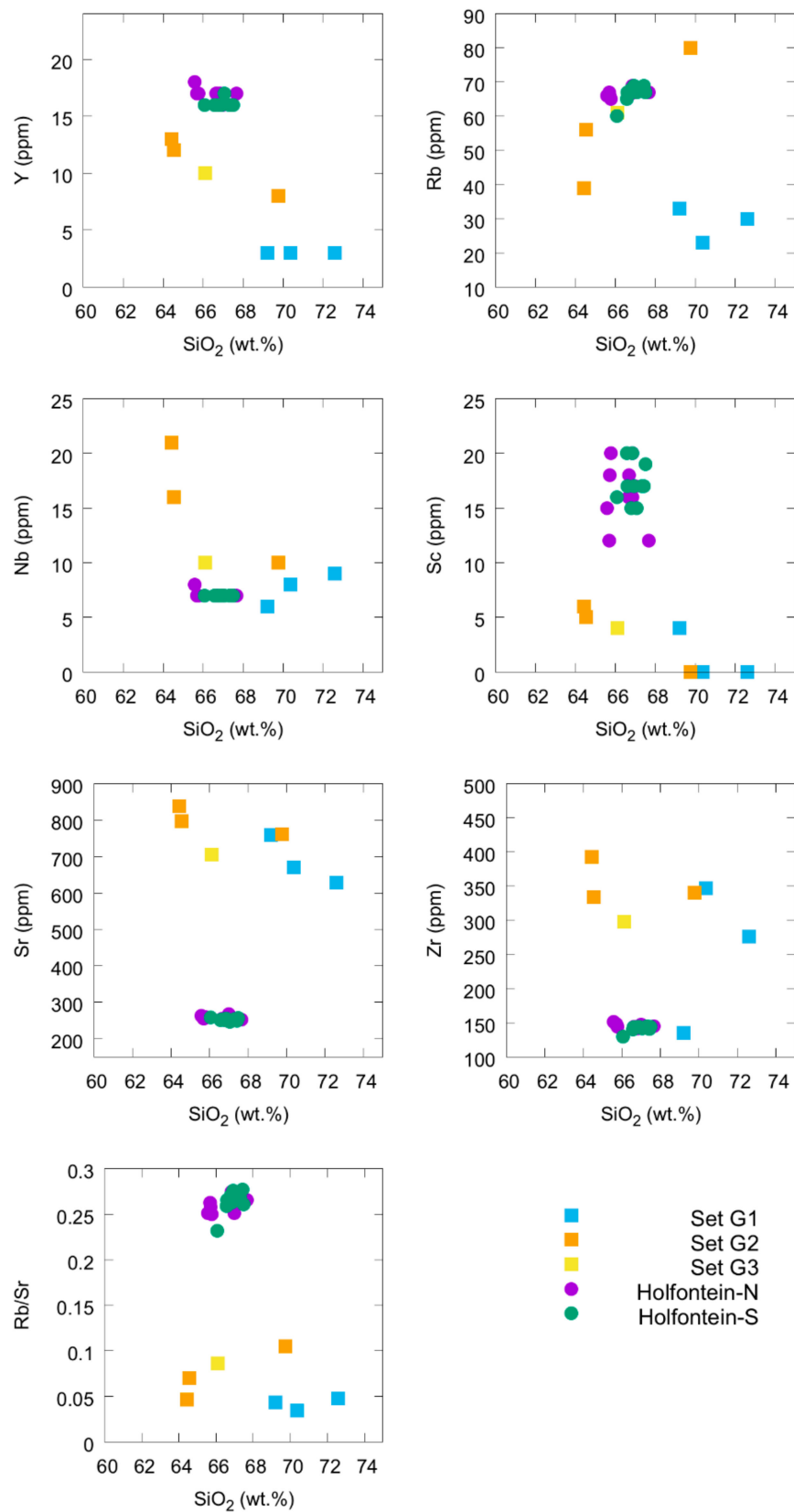


Figure 13. Granophyre and host granite trace element compositions vs. SiO₂.

4.6. Oxygen Isotopes

The average $\delta^{18}\text{O}$ value for the Holfontein Granophyre Dikes obtained in this work was 7.5‰, with no differences between HGD-N and HGD-S (Table 1, Figure 14). These data agree with previously published $\delta^{18}\text{O}$ values for Holfontein [30], namely, 7.6‰, which is close to the average of the present data. There was no correlation between the $\delta^{18}\text{O}$ value and any compositional parameter. Two samples (HPG18-5 and 10) were outliers and had $\delta^{18}\text{O}$ values (8.6‰ and 8.7‰) that were about 1‰ higher than the average.

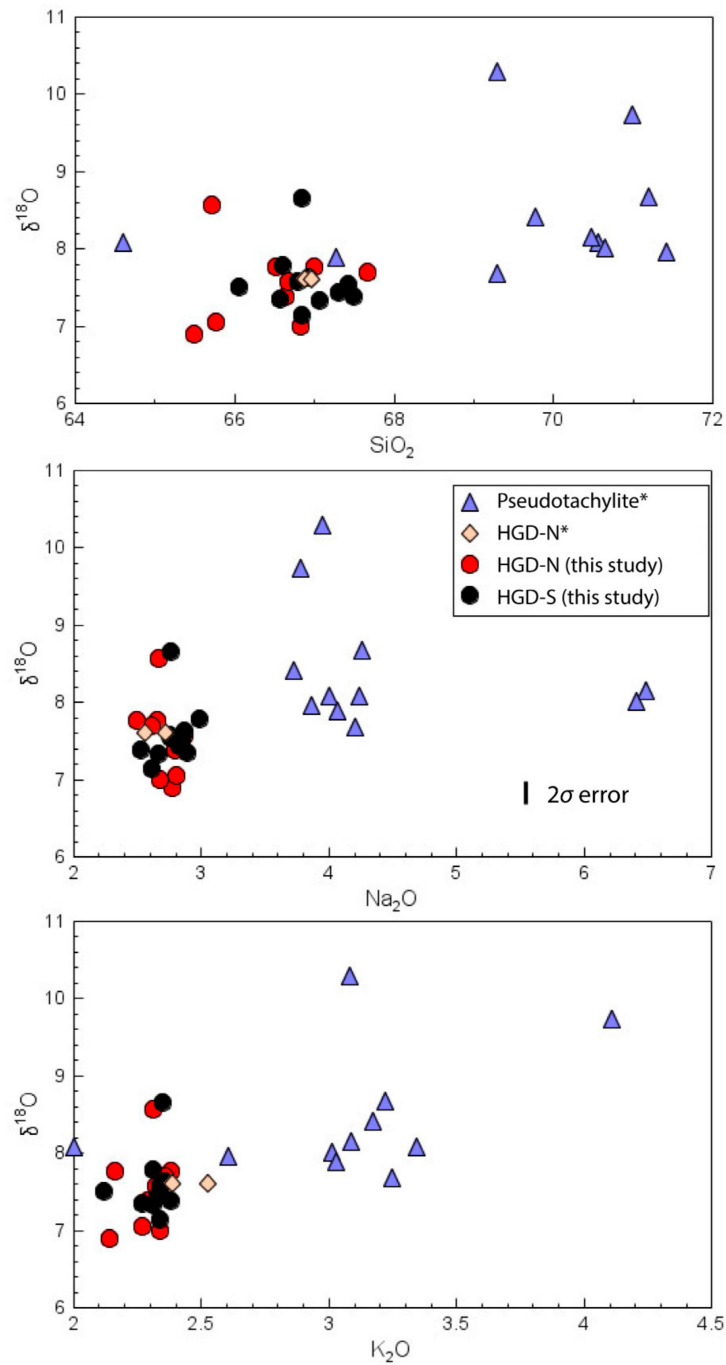


Figure 14. Plots of the $\delta^{18}\text{O}$ value vs. SiO_2 , Na_2O , and K_2O for granophyre samples. * Data points for HGD-N* and pseudotachylite veins from the Vredefort Impact Structure from [30].

5. Discussion

5.1. ERT Profiles and Magnetics

The inverse resistivity models obtained from the ERT data indicated that on all measured lines along the dike, the highly resistive material corresponding to granophyre dikes disappeared at shallow depths below the surface. The resistive zones associated with the HGD-S and HGD-N dikes respectively disappeared at depths of <5 m and <1.5 m below the surface. This is comparable to the resistivity profiles at the Daskop dike that also demonstrated that the highly resistive material disappears 2–3 m below the surface [31] and is interpreted to represent a lower termination of the granophyre material.

In contrast to the resistivity profiles at Daskop, there was resistive material at 5–20 m underneath lines P03 and P04. The nature of this resistive material is currently unknown, but it may correspond to a massive buried pseudotachylite body, similar to the massive pseudotachylite observed at the Leeukop or Otavi quarries [32]. On a recent field excursion to Vredefort from 6–11 October 2020, a significant construction project directly northwest of Holfontein Granophyre Dikes was underway, with trenches that were several hundreds of meters long and 2–3 m deep dug in various orientations to install underground piping for a new township development project (Figure 15A). Pervasive pseudotachylite networks that were several meters thick were found throughout these trenches and appeared to be more competent than the weathered and loose host granite material (Figure 15B). The presence of these large compact pseudotachylite melt bodies could explain the resistive material observed in the resistivity profiles.

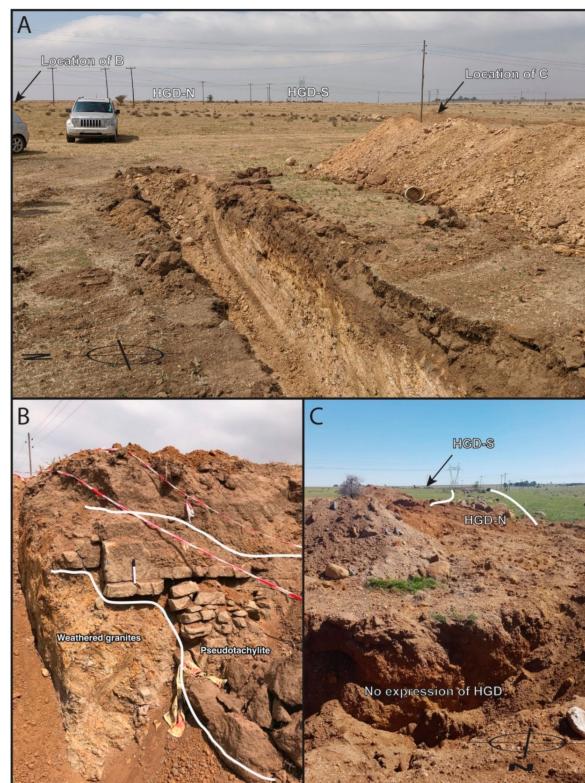


Figure 15. Field photographs showing construction trenching in the vicinity of the Holfontein Granophyre Dike. (A) Southeast-facing photograph of a construction trench with marked locations of the figure inset's B and C and segments HGD-N and HGD-S. (B) Photograph of a construction trench northwest of the Holfontein site. Exposed in the trench are weathered granitoid rocks that are highly friable and massive pseudotachylite bodies that remain rigid. Such pseudotachylite bodies are exposed at numerous places within the working trenches. Note the marker (14 cm) for scale. (C) A south-facing photograph showing the trench wall, which transected the HGD-N at the location of the former pigsty.

The magnetic anomalies observed to the west and east of HGD-N are typical of the shocked Archean basement rocks in the core of the Vredefort Impact Structure, which display magnetic anomalies with a wide range of wavelengths that often do not coincide with the surface geology [31]. This inconsistency between the surface geology and the recorded magnetic data is due to the intense and random magnetization of the shocked Archean rocks (on scales from less than a few centimeters to tens of kilometers) in the central part of the Vredefort Impact Structure, which has been discussed extensively (e.g., [33,34]). References [35,36] suggested that the peculiar magnetic properties of the basement rocks might be related to the presence of ultra-fine-grained (<5 μm) magnetite grains formed during an impact along shock-induced PDFs in quartz. In contrast to the shocked basement rocks, rocks produced from shock melting (pseudotachylite and granophyre) display normal induced and remanent magnetization with coherent magnetic vectors that are consistent with the paleomagnetic pole at the time of impact [34,37–39]).

5.2. Oxygen Isotopes

The new data are consistent with previous work by [30] that showed that two samples of granophyre (average 7.5‰) had lower $\delta^{18}\text{O}$ values than the pseudotachylite vein material (average $8.5 \pm 0.3\%$) or the host granite gneiss from the core ($8.6 \pm 0.8\%$). It should be noted that even though the granophyre dikes are >2 Ga, they are extremely fresh and contain very little water (<0.3 wt.% [30]). This means that a low-temperature surface alteration did not occur and would not have affected the $\delta^{18}\text{O}$ values.

The outlying $\delta^{18}\text{O}$ values of the granophyre did not correlate with the bulk composition (Figure 14). It is, therefore, unlikely that the cause for the higher $\delta^{18}\text{O}$ values was the presence or incorporation of clast material, unless the bulk composition of the clasts was the same as the melt that formed the dike, which is a possibility considering the clustering of compositions in Figure 10A. It is, however, more likely that the elevated $\delta^{18}\text{O}$ values were related to low-temperature alteration of the dikes with high $\delta^{18}\text{O}$, which increased the $\delta^{18}\text{O}$ value. A lack of correlation between $\delta^{18}\text{O}$ and Loss On Ignition (LOI) is normal, even in variably altered suites of igneous rocks [40].

Harris et al. [30] suggested that the difference in the $\delta^{18}\text{O}$ values between the granophyre and the pseudotachylite could be due to a combination of (i) inadequate sampling; (ii) differences in the degree of (non-eutectic) melting, with granophyre having higher input of mafic minerals, which have inherently lower $\delta^{18}\text{O}$ values; (iii) a component from the meteorite in granophyre with a lower $\delta^{18}\text{O}$ value. The present study greatly expanded the number of samples, therefore demonstrating that explanation (i) is not satisfactory. If granophyre dikes and pseudotachylite veins both represent bulk melts, then explanation (ii) is not possible unless the source material of the granophyre had a higher component of mafic minerals. It is possible that the granophyre at this location contained a greater greenstone belt (volcanic) or dolerite component, which would have had a lower $\delta^{18}\text{O}$, alkalis, and SiO_2 . Explanation (iii) is very unlikely given that [41] concluded that the granophyre contained only 0.2% of a chondrite meteorite component. Most of the ordinary chondrites have $\delta^{18}\text{O}$ values between 3‰ and 6‰ (e.g., [42]) and an addition of <1% of such material would make no measurable difference to a magma with a $\delta^{18}\text{O}$ value of 8‰ to 9‰. Given these constraints, the pseudotachylite veins were most consistent with local, frictional melting of the nearby OGG and ILG granite gneiss, as has been previously suggested [43].

5.3. Comparison of the Dike Segments

Although granophyre dikes have often been considered homogeneous in previous literature (see [25]), the HGD-N and HGD-S dike segments display significant variability in terms of their textures, internal features, and percentage of lithic clasts. HGD-N has spherulitic textures, which is indicative of supercooling [44] and were absent at HGD-S. HGD-S, however, had fluid escape pegmatitic veins that were absent in HGD-N [13]. Additionally, HGD-S had a high abundance of lithic clasts (typically found on the northern

margin of the dike), but HGD-N was clast-poor. These textural differences are possibly suggestive of different formation conditions of the dike segments, such as whether the HDG-N had crystallized at the higher stratigraphic level, and the HGD-S is likely the very bottom of the dike.

In contrast to the textural evidence, the geochemistry of the two dike segments was indistinguishable. The major and trace element geochemistry and the oxygen isotope composition were suggestive of the two dike segments having the same provenance. Given that HGD-S had a much higher visible clast population, this would seem to indicate that a similar percentage of clasts contributed to the total volume of the material in both dike segments. HGD-N, therefore, may have been more efficient at assimilating lithic clasts, i.e., may have cooled down slower than HGD-S.

The resistivity models showed that both HGD-N and HGD-S had shallow penetration depths. HGD-N had a very shallow penetration depth (<1.5 m) and a disaggregated appearance in the resistivity models, which agrees with the observed disaggregation at the surface. The shallow penetration depth was confirmed via trenching. HGD-S was characterized by a more compact zone with high resistivities and a larger penetration depth (<5 m). The compact appearance of HGD-S in the resistivity models agrees with the observed compact nature of the outcrop of this dike segment.

All of the host granite samples examined in this study exhibited deformation features, but the style of deformation features varied relative to their position to the dike segments. Sample HGP18-G1, for example, was mylonitized and sample 18.12.G2 was a charnockite, both of which lay directly between the two dike segments. North-dipping foliations were also recorded adjacent to 18.12.G2. Sample 18.12.G3 collected to the west of HGD-N had no apparent foliation, but diffuse grain boundaries, indicating that processes that led to the mylonitization and charnockitization of the granites were restricted to the zone between the two dike segments. Mylonitization and foliation, specifically, are suggestive of deformation associated with fault activity.

At the surface, HGD-N and HGD-S were sub-parallel but curved away from each other from their closest point (Figure 2). This spatial arrangement indicates that the two dike segments could have formed as one dike that was subsequently displaced after solidification by a fault with a sinistral sense of movement. The interpretation of a single melt body was supported by the homogeneous chemistry of the segments. The variation in textures between the two segments may represent crystallization of the dike segments at different depths, or be linked to variations in texture or clast abundance along the strike of the dike, as is observed at the Daskop dike [31,45]. Therefore, the spatial arrangement of the dikes may be interpreted to be either a sinistral or oblique-slip fault. Based on the petrographic, structural, and spatial observations, the shallow penetration depth of the dike in both segments should be interpreted in the context of a structurally active environment. For HGD-N and HGD-S to have similar penetration depths but different textural characteristics, segmentation of the dike could have been accomplished on an oblique plane of motion, which would have shifted HGD-N downward relative to the HGD-S segment. Such movement would explain the characteristics observed at HGD-N, which are consistent with crystallization at a slightly higher level within a dike. The shallow penetration depth of HGD-S, in contrast, could represent the lowermost extent of the dike. On a recent field trip on 2 December 2020, construction workers dug a trench across HGD-N at the location of the pigsty. It can be seen clearly that there was no granophyre expressed at depth, confirming the observations seen in the ERT profiles (Figure 15C).

Another possibility is that textural and clast variability between the two segments could represent variability along the strike of the dike. In this case, the fault would have displaced the dikes horizontally through pure strike-slip motion. Based on our observations, it is clear that sinistral strike-slip motion resulted in the spatial arrangement of the dike segments, but we cannot definitively constrain any component of vertical motion without a better understanding of the primary along-strike textural and clast variability of the granophyre dike segments.

5.4. Timing of the Faulting

The hypothesized fault that displaced the Holfontein Granophyre Dike into two segments could only occur after the dike crystallized.

There are no significant post-impact tectonic events that have affected the Vredefort Impact Structure [10,11]. The granophyre dikes have long been known to have been emplaced at the latest stages of development of the Vredefort Impact Structure based on the fact that the dikes cross-cut the uplifted collar rocks (e.g., [24]). The core dikes were likely derived from a homogenized melt sheet [2], and thus must have formed after the initial cratering process. The emplacement mechanism of the dikes is not fully understood [25], but is generally thought to have been associated with the opening of fractures deep in the crust, either by hydrostatic pressure-opening faults [46] or by faults opening through a process ongoing during post-impact crustal adjustment (e.g., [15]). The offset of the HGD after crystallization demonstrates that faults were developing deep within the crust under the Vredefort Impact Structure also after the granophyre melt emplacement and crystallization occurred. This later faulting was not associated with melt migration or melt formation, and so can be interpreted as either distinct from the faulting that allowed the granophyre dikes to be emplaced, or as the same physical process, but occurring after solidification of the melt sheet was completed, which could have required 100,000 years [47].

5.5. Observations Based on a Comparison of the Datasets

Taken together, the various lines of evidence in this study reveal a consistent story regarding the emplacement and post-emplacement history of the Holfontein Granophyre Dike. The aerial photography and field investigations revealed two segments of the dike, namely, Holfontein-N and Holfontein-S, that were offset from one another. The petrography, major element, trace element, and isotopic geochemistry consistently demonstrated that the compositions of these segments were indistinguishable from one another. Furthermore, the highly resistive material, i.e., granophyre, disappeared at a shallow depth below the surface, which was confirmed by the trenching that had taken place at the site. Around the dike, the host granitoids had two distinct compositions, with the samples taken to the west of the dike segments being more silicic and having a lower An content than those to the east of the dike segments.

These various lines of evidence can be interpreted as the emplacement of a single dike at a late stage during the development of the Vredefort Impact Structure, with the melt being homogeneous (likely as a result of a homogeneous source for the melt; [2]). The emplacement of the dike likely required a pre-existing fracture to be present for the dike to exploit such that the host granites may have been offset from one another prior to or coeval with the emplacement of the dike. The present-day surface may represent the deepest depth to which the dike could penetrate, as hypothesized by [31].

The faulting of the dike into the N and S segments could only have taken place after the dike had cooled and crystallized. This faulting must have been driven by a process during the post-impact readjustment of the crust, in which the crater floor was gradually raised over a protracted period. The same process that horizontally displaced the dike could also explain the disappearance of the resistivity signal of the granophyre at shallow depths such that this process may have resulted in vertical segmentation of the dike as well. In effect, this would mean that the lowermost extent of the dike may also represent another structural discontinuity, similar to the segmentation observed with regard to the Sudbury Offset Dikes [48,49].

6. Conclusions

The geophysical, geochemical, petrographic, and geospatial evidence presented here suggests that the Holfontein Granophyre Dike intruded as a single dike that was subsequently segmented by an ENE–WSW sinistral strike-slip fault zone that must have occurred during a late stage of the impact process (Figure 16). HGD-N and HGD-S are geochemically

identical, originating from the same melt source, but vary in texture and clast abundance. The HGD-N segment represents either a slightly stratigraphically higher portion of the dike that was displaced downward relative to HGD-S to be at the same stratigraphic horizon or a texturally different segment of the dike with a different clast abundance along the strike. Both segments of the dike terminate at a shallow depth below the surface, representing a lowermost fault surface for the HGD-N and the lower limit of the dike emplacement for HGD-S (Figure 16).

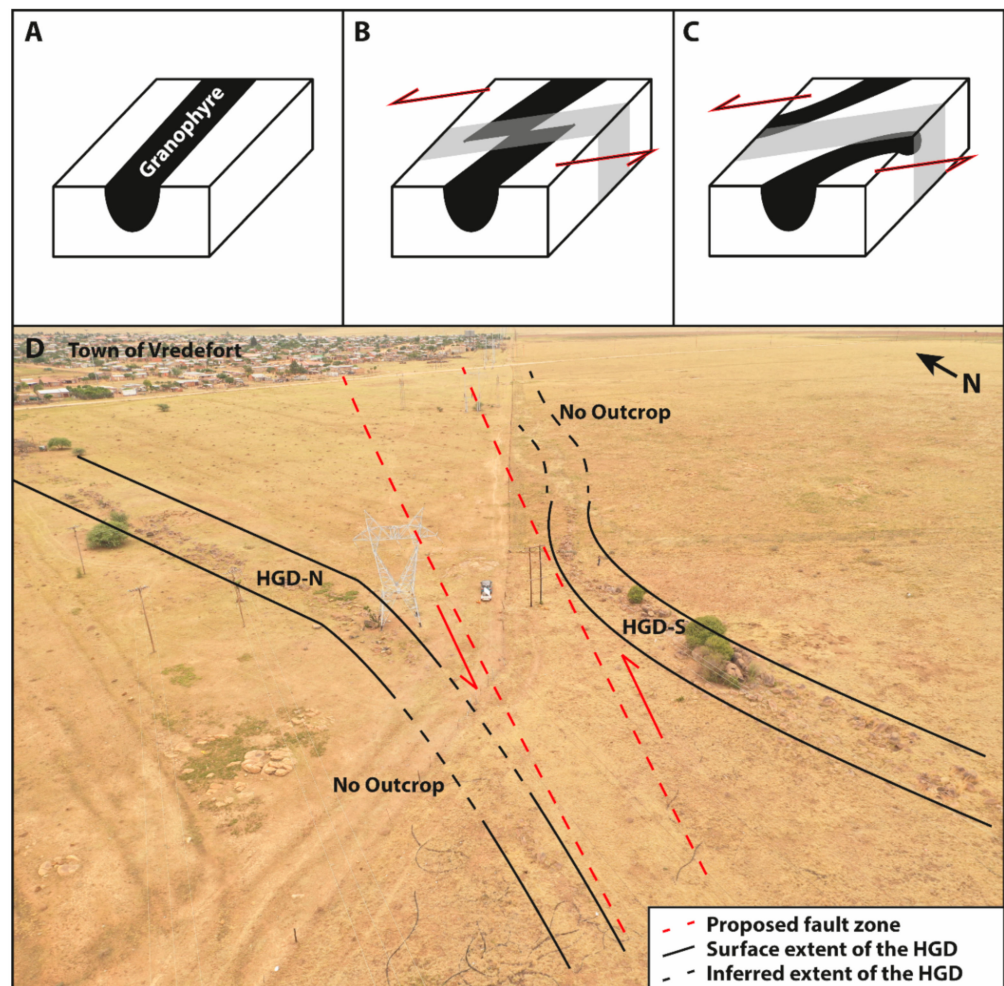


Figure 16. Schematic diagrams and annotated expression of the Holfontein Granophyre Dike with the proposed strike-slip sinistral fault zone. Schematic diagrams A–C show intact (A), intermediate (B), and final (C) stages of shearing of the HGD. (D) Aerial photograph of the HGD showing the proposed orientation of the fault zone.

Author Contributions: Conceptualization, M.D.C.; methodology, M.D.C., E.K., M.S.H., and F.F.; formal analysis, C.H.; investigation, M.D.C., E.K., M.S.H., and F.F.; writing—original draft preparation, M.D.C., E.K., M.S.H., F.F., and C.H.; writing—review and editing, M.D.C., E.K., M.S.H., F.F., and C.H. All authors have read and agreed to the published version of the manuscript.

Funding: This work was produced within the framework of the interdisciplinary project GRAVITAS (“Geological Research and Analysis of Vredefort Impact with Timely Anthropological Studies”), funded by the Directorate for Research Development, University of the Free State, 2019–2020. The oxygen isotope analyses were funded from a National Research Foundation (NRF) incentive grant to C.H.

Data Availability Statement: The aerial imagery presented in this study is openly available in Figshare at <https://doi.org/10.38140> (accessed on 28 December 2020), reference number ufs.13698817.v2.

Acknowledgments: The manager of the property where the HGD-S is located, Gerhard Swanepoel, is thanked for the outcrop access permission. Megan Purchase is acknowledged for obtaining the XRF results. Sherissa Roopnarain is thanked for her assistance with the O isotope work. The reviewers are thanked for their constructive reviews.

Conflicts of Interest: The authors declare no conflict of interest.

References

1. Grieve, R.; Therriault, A. Vredefort, Sudbury, Chicxulub: Three of a Kind? *Annu. Rev. Earth Planet. Sci.* **2000**, *28*, 305–338. [[CrossRef](#)]
2. Huber, M.S.; Kovaleva, E.; Riller, U. Modeling the geochemical evolution of impact melts in terrestrial impact basins: Vredefort granophyre dikes and Sudbury offset dikes. *Meteorit. Planet. Sci.* **2020**, *55*, 2320–2337. [[CrossRef](#)]
3. Therriault, A.M.; Reimold, W.U.; Reid, A.M. Field relations and petrography of the Vredefort Granophyre. *S. Afr. J. Geol.* **1996**, *99*, 1–21.
4. McCarthy, T.; Stanistreet, I.; Robb, L. Geological studies related to the origin of the Witwatersrand Basin and its mineralization: An introduction and a strategy for research and exploration. *S. Afr. J. Geol.* **1990**, *93*, 1–4.
5. Therriault, A.M.; Grieve, R.A.F.; Reimold, W.U. Original size of the Vredefort structure: Implications for the geological evolution of the Witwatersrand Basin. *Meteorit. Planet. Sci.* **1997**, *32*, 71–77. [[CrossRef](#)]
6. Pilles, E.A.; Osinski, G.R.; Grieve, R.A.F.; Smith, D.; Bailey, J. Formation of large-scale impact melt dikes: A case study of the Foy Offset Dike at the Sudbury impact structure, Canada. *Earth Planet. Sci. Lett.* **2018**, *495*, 224–233. [[CrossRef](#)]
7. Bailey, J.; Lafrance, B.; McDonald, A.M.; Fedorowich, J.S.; Kamo, S.; Archibald, D.A. Mazatzal-Labradorian-age (1.7–1.6 Ga) ductile deformation of the South Range Sudbury impact structure at the Thayer Lindsley mine, Ontario. *Can. J. Earth Sci.* **2004**, *41*, 1491–1505. [[CrossRef](#)]
8. Card, K.D.; Gupta, V.K.; McGrath, P.H.; Grant, F.S. The Sudbury Structure: Its Regional Geological and Geophysical Setting. In *The Geology and Ore deposits of the Sudbury Structure*; Ontario Geological Survey: Toronto, ON, Canada, 1984; pp. 25–44.
9. Moser, D.E. Dating the shock wave and thermal imprint of the giant Vredefort impact, South Africa. *Geology* **1997**, *25*, 7–10. [[CrossRef](#)]
10. Simpson, C. The structure of the rim synclinorium of the Vredefort dome. *Trans. Geol. Soc. S. Afr.* **1978**, *81*, 115–121.
11. Colliston, W.P. A model of compressional tectonics for the origin of the Vredefort structure. *Tectonophysics* **1990**, *171*, 115–118. [[CrossRef](#)]
12. Therriault, A.M.; Reimold, W.U.; Reid, A.M. Geochemistry and impact origin of the Vredefort Granophyre. *S. Afr. J. Geol.* **1997**, *100*, 115–122.
13. Kovaleva, E.; Huber, M.S.; Zaccarini, F. Petrography and geochemistry of coarse-crystalline veins within Vredefort granophyre, Vredefort impact structure, South Africa. *S. Afr. J. Geol.* **2018**, *121*, 383–402. [[CrossRef](#)]
14. Cooper, M.R. Tectonic cycles in southern Africa. *Earth Sci. Rev.* **1990**, *28*, 321–364. [[CrossRef](#)]
15. Wichman, R.W.; Schultz, P.H. Floor-fractured crater models of the Sudbury Structure, Canada: Implications for initial crater size and crater modification. *Meteoritics* **1993**, *28*, 222–231. [[CrossRef](#)]
16. Lieger, D.; Riller, U. Emplacement history of Granophyre dikes in the Vredefort Impact Structure, South Africa, inferred from geochemical evidence. *Icarus* **2012**, *219*, 168–180. [[CrossRef](#)]
17. Huber, M.S.; Kovaleva, E.; Clark, M.D.; Fourie, F. Evaluating the emplacement mechanisms of Vredefort impact melt dikes. In Proceedings of the 11th Planetary Crater Consortium, Honolulu, HI, USA, 5–7 August 2020; p. 2.
18. Henkel, H.; Reimold, W.U. Integrated geophysical modelling of a giant, complex impact structure: Anatomy of the Vredefort Structure, South Africa. *Tectonophysics* **1998**, *287*, 1–20. [[CrossRef](#)]
19. Hart, R.J.; Welke, H.J.; Nicolaysen, L.O. Geochronology of the deep profile through Archean basement at Vredefort, with implications for early crustal evolution. *J. Geophys. Res.* **1981**, *86*, 10663–10680. [[CrossRef](#)]
20. Stepto, D. The geology and gravity field in the central core of the Vredefort structure. *Tectonophysics* **1990**, *171*, 75–103. [[CrossRef](#)]
21. Hart, R.J.; Andreoli, M.A.G.; Tredoux, M.; De Wit, M.J. Geochemistry across an exposed section of Archean crust at Vredefort, South Africa: With implications for mid-crustal discontinuities. *Chem. Geol.* **1990**, *82*, 21–50. [[CrossRef](#)]
22. Bisschoff, A.A. The history and origin of the Vredefort Dome (South Africa). *S. Afr. J. Sci.* **1988**, *84*, 413–417.
23. Lana, C.; Gibson, R.L.; Kisters, A.F.M.; Reimold, W.U. Archean crustal structure of the Kaapvaal craton, South Africa - evidence from the Vredefort dome. *Earth Planet. Sci. Lett.* **2003**, *206*, 133–144. [[CrossRef](#)]
24. Bisschoff, A.A. The dioritic rocks of the Vredefort Dome. *S. Afr. J. Geol.* **1972**, *75*, 31–45.
25. Huber, M.S.; Kovaleva, E. Identifying Gaps in the Investigation of the Vredefort Granophyre Dikes: A Systematic Literature Review. *Geosciences* **2020**, *10*, 306. [[CrossRef](#)]
26. Harris, C.; le Roux, P.; Cochrane, R.; Martin, L.; Duncan, A.R.; Marsh, J.S.; le Roex, A.P.; Class, C. The oxygen isotope composition of Karoo and Etendeka picrites: High $\delta^{18}\text{O}$ mantle or crustal contamination? *Contrib. Mineral. Petrol.* **2015**, *170*, 8. [[CrossRef](#)]
27. Bas, M.J.L.; Maitre, R.W.L.; Streckeisen, A.; Zanettin, B. A chemical classification of volcanic rocks based on the total alkali-silica diagram. *J. Petrol.* **1986**, *27*, 745–750. [[CrossRef](#)]

28. Frost, B.R.; Barnes, C.G.; Collins, W.J.; Arculus, R.J.; Ellis, D.J.; Frost, C.D. A Geochemical Classification for Granitic Rocks. *J. Petrol.* **2001**, *42*, 2033–2048. [[CrossRef](#)]
29. Barker, F. Trondhjemite: Definition, Environment and Hypotheses of Origin. In *Developments in Petrology*; Elsevier Scientific Publishing Company: Amsterdam, The Netherlands, 1979; Volume 6, pp. 1–12.
30. Harris, C.; Fourie, D.S.; Fagereng, A. Stable isotope evidence for impact-related pseudotachylite formation at Vredefort by local melting of dry rocks. *S. Afr. J. Geol.* **2013**, *116*, 101–118. [[CrossRef](#)]
31. Fourie, F.D.; Huber, M.S.; Kovaleva, E. Geophysical characterization of the Daskop granophyre dyke and surrounding host rocks, Vredefort impact structure, South Africa. *Meteorit. Planet. Sci.* **2019**, *54*, 1579–1593. [[CrossRef](#)]
32. Reimold, W.U.; Hoffmann, M.; Zaag, P.T.; Schmitt, R.-T.; Hauser, N.; Mohr-Westerheide, T. A geochemical contribution to the discussion about the genesis of impact-related pseudotachylitic breccias: Studies of PTB in the Otavi and Kudu Quarries of the Vredefort Dome support the “In Situ Formation” hypothesis. *S. Afr. J. Geol.* **2016**, *119*, 453–472. [[CrossRef](#)]
33. Carporzen, L.; Gilder, S.A.; Hart, R.J. Palaeomagnetism of the Vredefort meteorite crater and implications for craters on Mars. *Nature* **2005**, *435*, 198–201. [[CrossRef](#)]
34. Hart, R.; Carporzen, L.; Gilder, S.; Muundjua, M.; Galdeano, A. Paleomagnetism of Vredefort: Plasma, Lightning, or? In Proceedings of the AGU Fall Meeting Abstracts, San Francisco, CA, USA, 5–9 December 2005; p. GP33A-0095.
35. Hart, S.R.J.; Cloete, M. Impact related magnetic rocks from the Vredefort Impact Structure. *Meteorit. Planet. Sci. Suppl.* **1999**, *34*, A50.
36. Cloete, M.; Hart, R.J.; Schmid, H.K.; Drury, M.; Demanet, C.M.; Sankar, K.V. Characterization of magnetite particles in shocked quartz by means of electron- and magnetic force microscopy: Vredefort, South Africa. *Contrib. Mineral. Petrol.* **1999**, *137*, 232–245. [[CrossRef](#)]
37. Hart, R.J.; Hargraves, R.B.; Andreoli, M.A.G.; Tredoux, M.; Moctar Doucouré, C. Magnetic anomaly near the center of the Vredefort structure: Implications for impact-related magnetic signatures. *Geology* **1995**, *23*, 277. [[CrossRef](#)]
38. Rao, M. Intense random magnetism in the vredefort dome. *Geol. Soc. India* **2006**, *68*, 154.
39. Muundjua, M.; Hart, R.J.; Gilder, S.A.; Carporzen, L.; Galdeano, A. Magnetic imaging of the Vredefort impact crater, South Africa. *Earth Planet. Sci. Lett.* **2007**, *261*, 456–468. [[CrossRef](#)]
40. Harris, C.; Smith, H.S.; Milner, S.C.; Erlank, A.J.; Duncan, A.R.; Marsh, J.S.; Ikin, N.P. Oxygen isotope geochemistry of the Mesozoic volcanics of the Etendeka Formation, Namibia. *Contrib. Mineral. Petrol.* **1989**, *102*, 454–461. [[CrossRef](#)]
41. Koeberl, C.; Reimold, W.U.; Shirey, S.B. Re-Os isotope and geochemical study of the Vredefort Granophyre: Clues to the origin of the Vredefort structure, South Africa. *Geology* **1996**, *24*, 913–916. [[CrossRef](#)]
42. McKeegan, K.D.; Leshin, L.A. Stable isotope variations in extraterrestrial materials. *Rev. Mineral. Geochem.* **2001**, *43*, 278–318. [[CrossRef](#)]
43. Reimold, W.U.; Hauser, N.; Hansen, B.T.; Thirlwall, M.; Hoffmann, M. The impact pseudotachylitic breccia controversy: Insights from first isotope analysis of Vredefort impact-generated melt rocks. *Geochim. Cosmochim. Acta* **2017**, *214*, 266–281. [[CrossRef](#)]
44. Lafrance, B.; Bygnes, L.; McDonald, A.M. Emplacement of metabreccia along the Whistle offset dike, Sudbury: Implications for post-impact modification of the Sudbury impact structure. *Can. J. Earth Sci.* **2014**, *51*, 466–484. [[CrossRef](#)]
45. Huber, M.S.; Kovaleva, E.; Clark, M.D.; Prevec, S.A. Inhomogeneous distribution of lithic clasts within the Daskop Granophyre Dike, Vredefort Impact Structure: Implications for emplacement of impact melt in large impact structures. In *Large Meteorite Impacts and Planetary Evolution VI, Geological Society of America Special Paper 550 (In Press)*; Reimold, W.U., Koeberl, C., Eds.; The Geological Society of America: Boulder, CO, USA, 2021.
46. Prevec, S.A.; Büttner, S.H. Multiphase emplacement of impact melt sheet into the footwall: Offset dykes of the Sudbury Igneous Complex, Canada. *Meteorit. Planet. Sci.* **2018**, *53*, 1301–1322. [[CrossRef](#)]
47. Zieg, M.J.; Marsh, B.D. The Sudbury Igneous Complex: Viscous emulsion differentiation of a superheated impact melt sheet. *Bull. Geol. Soc. Am.* **2005**, *117*, 1427–1450. [[CrossRef](#)]
48. Lightfoot, P.G.; Keays, R.R.; Morrison, G.G.; Bite, A.; Farrell, K.P. Geochemical relationships in the sudbury igneous complex: Origin of the main mass and offset dikes. *Econ. Geol.* **1997**, *92*, 289–307. [[CrossRef](#)]
49. Lightfoot, P.C.; Keays, R.R.; Morrison, G.G.; Bite, A.; Farrell, K.P. Geologic and geochemical relationships between the contact sublayer, inclusions, and the main mass of the Sudbury Igneous Complex; a case study of the Whistle Mine Embayment. *Econ. Geol.* **1997**, *92*, 647–673. [[CrossRef](#)]